Marine Structures 83 (2022) 103190

Contents lists available at ScienceDirect

Marine Structures

journal homepage: www.elsevier.com/locate/marstruc

Application of Arbitrary Lagrangian–Eulerian strips with fully nonlinear wave kinematics for force estimation

Csaba Pákozdi [a], Arun Kamath [b,*], Weizhi Wang [b], Hans Bihs [b]

[a] SINTEF Ocean, Otto Nielsens veg 10, Trondheim, Norway
[b] Department of Civil and Environmental Engineering, Norwegian University of Science and Technology, NTNU Trondheim, Norway

ARTICLE INFO

Keywords:
Slender cylinder
Irregular breaking waves
REEF3D
FNPF
ALE

ABSTRACT

The initial design of offshore constructions generally uses a combination of model tests and second-order wave theory to reconstruct the wave kinematics to determine wave forces using the Morison equation. This routine becomes difficult to apply to steep waves without model test data where the second-order theory is not valid. In this article, a novel approach combining a fully nonlinear numerical wave tank (NWT) using the σ-grid with strip theory and the Morison equation in an Arbitrary Lagrangian–Eulerian (ALE) framework is presented. This provides improved wave kinematics from the nonlinear numerical wave tank, an improved representation of the instantaneous velocity field associated with the instantaneous location of the free surface, making an accurate estimation of the wave hydrodynamics of highly nonlinear and breaking waves possible at a reasonable computational cost.

The method is verified by comparing the calculated wave kinematics for a fifth-order Stokes wave with the analytical solution. The procedure for the estimation of the hydrodynamic loads on a cylinder is validated using comparisons with model test data for wave forces on a cylinder due to regular, irregular and focussed waves. A good agreement is seen for the estimated wave forces, including for the breaking waves in the irregular wave train. Some overestimation of the wave forces due to irregular waves is seen due to the frequency-independent force coefficient used in the Morison equation. The results demonstrate the potential of the ALE method combined with a nonlinear NWT to evaluate a three-hour irregular sea state simulation and generate wave loading statistics for the initial stochastic design of offshore structures without model test data.

1. Introduction

The accurate evaluation of wave hydrodynamics, especially wave forces due to breaking waves and extreme wave statistics is essential for safe and economic design of marine constructions such as those for the offshore wind and aquaculture industries [1]. The Morison equation is generally used in the design of slender structures in such constructions to relate the fluid acceleration and velocity to the wave forces through empirical coefficients. The analytical approach using the second-order wave theory combined with data from model tests is generally used to estimate the necessary wave kinematics [2,3]. Although useful in several cases, this approach is difficult to apply to steep, breaking waves, extreme waves and extreme wave statistics which are outside the range of validity of the second-order wave theory [4]. Since these environmental loadings determine the ultimate limit state and survivability of the structure, accurate determination of these loadings is essential [5,6].

* Corresponding author.
E-mail addresses: csaba.pakozdi@sintef.no (C. Pákozdi), arun.kamath@ntnu.no (A. Kamath), weizhi.wang@ntnu.no (W. Wang), hans.bihs@ntnu.no (H. Bihs).

https://doi.org/10.1016/j.marstruc.2022.103190
Received 22 June 2021; Received in revised form 17 December 2021; Accepted 15 February 2022
Available online 4 March 2022

Study of irregular waves in the field and large-scale experiments have provided a large amount information about the wave kinematics under steep breaking waves [7,8] along with analytical expressions to represent steep nonlinear waves [9]. Numerical simulations incorporating higher-order wave kinematics can provide further insight into the wave hydrodynamics. For example, computational fluid dynamics (CFD) simulations based on the solution of the Navier–Stokes equations can deal with steep waves and wave breaking [10]. The high computational cost in such an approach has limited their extensive use for stochastic engineering design. Adapting numerical approaches that resolve the higher-order wave kinematics more efficiently to calculate the velocity field in the near-field is a promising alternative to CFD simulations. More efficient approaches using the higher order spectral method [11], coupled HOS and CFD simulations [12] and Boussinesq approaches have been proposed [13]. In the CFD approach, the complex free surface is directly accounted with most of the fluid hydrodynamics but at a considerable computational cost [14–16]. The potential theory-based approach is computationally more efficient but the inherent assumption of an inviscid, irrotational fluid restricts their utility to non-breaking waves as they become unstable when breaking waves are encountered.

From the perspective of estimation of wave loads on structures, procedures such as Wheeler stretching [17] makes some improvement to the estimation of the drag force, without any improvement to the inertia force estimation. In another approach, using the second-order wave theory with perturbation parameters to evaluate the wave kinematics at the free surface, the applicability of wave theory is extended to nonlinear waves by a limited extent [18,19]. Analytical solutions to determine higher-order loading due to wave diffraction [20,21] have been proposed along with semi-empirical approaches to evaluate the ringing response of offshore structures in irregular waves [22]. Extending the knowledge gained from these studies for long-crested waves, the new class of efficient numerical models mentioned above, can provide higher-order wave kinematics in nonlinear irregular sea states. This in combination with Morison equation can provide quick estimates of the wave forces on slender structures with reasonable accuracy, enabling further adoption of higher-order numerical modelling for stochastic design. The major challenge in the application of potential flow models to steep irregular sea states is the stability of the model when wave breaking occurs. Several solutions have been proposed to maintain the stability of the simulation when wave breaking is encountered while sufficiently accounting for the change in the wave kinematics [23,24]. This extends the applicability of efficient nonlinear potential flow models [25–27] to nonlinear irregular sea states in intermediate waters.

In order to use the nonlinear NWT wave kinematics to estimate the hydrodynamic loads, it is essential to obtain an accurate representation of the instantaneous velocity field associated with the free surface in the near-field. This makes it possible to use the Morison equation with the appropriate integration of the undisturbed velocity and acceleration at the location of the structure following strip theory. Due to the oscillatory flow, the wetted surface of the structure changes constantly and poses a challenge to the correct determination of the instantaneous velocity and acceleration fields associated with the free surface elevation at the location of the structure. This requirement is met with a nonlinear NWT employing a moving grid that follows the free surface, called the σ-grid. The Laplace equation is solved in this moving frame and is treated as an Arbitrary Lagrangian–Eulerian (ALE) framework [28]. The free surface motion is represented in a Lagrangian manner while maintaining the advantages from a Eulerian mesh [29]. Using the ALE kinematic description to calculate the wave kinematics directly provides the water particle velocity corresponding to the free surface elevation and coordinates at the location of the structure always represent the wetted surface, making the application of the Morison equations straightforward. This is a major advantage over using fixed Eulerian strips which undergo wetting and drying in an oscillatory flow.

In this paper, the ALE framework is used in conjunction with strip theory and the Morison equation to estimate the hydrodynamic load on a cylinder, with the REEF3D framework [30] for the numerical modelling. The nonlinear wave kinematics are obtained from the fully nonlinear potential flow model REEF3D::FNPF, which has previously been used to simulate steep nonlinear wave propagation [31–33]. The presented methodology is verified with analytical results for higher-order wave kinematics. The method is further validated for the estimation of global forces and moments using comparisons to model test data. The presented method can be used with higher-order regular or irregular waves. The procedure is used to estimate the total time derivative of the water particle velocity from the result of the NWT simulations without the structure to define the inertial forces in the Morison equation. The results show that a cubic spline interpolation based integration provides a good estimation of the global force and the moment, even with the use of constant force coefficients in the Morison equation for irregular waves with a limited number of strips sections.

2. Methodology

2.1. Nonlinear Wave Tank with σ-grid

The paper uses the NWT in the open-source model REEF3D::FNPF which solves the governing equations for fully nonlinear potential flow, the Laplace equation, on a σ-grid. The kinematic and dynamic boundary conditions must be fulfilled at all times at the free surface along with a seabed boundary condition in order to solve for the velocity potential Φ. The model enforces an impervious solid boundary at the bed. The Laplace equation with the boundary conditions is solved using a finite difference method on a σ-coordinate system. A σ-coordinate system deforms with the free surface and is flexible in the handling of irregular boundaries. The relationship between a Cartesian grid and a σ-coordinate is as follows:

$$\sigma = \frac{z + h(\mathbf{x})}{\eta(\mathbf{x}, t) + h(\mathbf{x})}. \tag{1}$$

The Laplace equation is discretised using a second-order central difference scheme and is solved using a parallelised geometric multi-grid pre-conditioned bi-conjugated gradient solver provided by the high-performance solver library, Hypre [34].

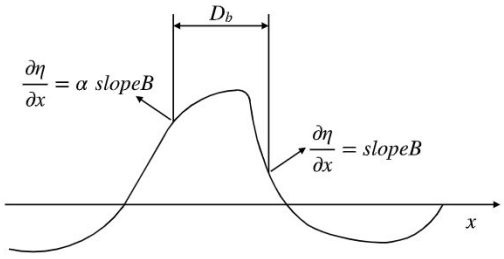

Fig. 1. Definition of the breaking wave model.

The convection terms at the free-surface are discretised with the fifth-order Hamilton–Jacobi weighted essentially non-oscillatory (WENO) scheme [35]. A WENO discretisation stencil is based on the smoothness of three local ENO stencils. The local stencil with the highest smoothness is assigned the highest weight and contributes most significantly to the solution and enables the handling of large gradients without instability. For the time treatment, a third-order accurate TVD Runge–Kutta scheme [36] is used with a constant time step. The model is fully parallelised following the domain decomposition strategy. Ghost cells are used to exchange information between adjacent domains and are updated with the values from the neighbouring processors using the Message Passing Interface (MPI). Further details regarding the numerical model are found in [37].

Wave generation in the NWT is handled using a Neumann boundary condition. Here, the spatial derivatives of the velocity potential are prescribed according to the wavemaker kinematics with help of ghost cells. Wave generation can be based on input analytical wave spectrum, wave theory or wavemaker motion. In this paper, the measured piston motion from the experiments is used to generate the incident waves in the NWT and obtain a time series comparison. An active absorption method is used to mitigate wave reflection as presented in Miquel et al. [38].

In order to avoid numerical breakdown that can occur in Laplace equation-based models when wave breaking events occur, a wave breaking dissipation algorithm is included in the model. In this way, the model simulates the free surface elevation up to the point of wave breaking accurately. The wave breaking algorithm is then activated at this stage when an overturning wave crest is expected and which would result in numerical breakdown. This algorithm accounts for the reduction in the wave energy to mimic wave breaking, without representing the overturning wave crest. The empirical breaking wave model presented by Baquet et al. [24] is implemented in REEF3D::FNPF. The dynamic and kinematic free surface conditions are modified and extended by one extra element to mimic the energy dissipation due to a breaking wave as follows:

$$\begin{aligned}
\frac{\partial \eta}{\partial t} &= -\frac{\partial \eta}{\partial x}\frac{\partial \widetilde{\Phi}}{\partial x} - \frac{\partial \eta}{\partial y}\frac{\partial \widetilde{\Phi}}{\partial y} + \widetilde{\omega}\left(1 + \left(\frac{\partial \eta}{\partial x}\right)^2 + \left(\frac{\partial \eta}{\partial y}\right)^2\right) + \nu_B(x,t)\left(\frac{\partial^2 \eta}{\partial x^2}\right) \\
\frac{\partial \widetilde{\Phi}}{\partial t} &= -\frac{1}{2}\left[\left(\frac{\partial \widetilde{\Phi}}{\partial x}\right)^2 + \left(\frac{\partial \widetilde{\Phi}}{\partial y}\right)^2 - \widetilde{\omega}^2\left(1 + \left(\frac{\partial \eta}{\partial x}\right)^2 + \left(\frac{\partial \eta}{\partial y}\right)^2\right)\right] - g\eta + \nu_B(x,t)\left(\frac{\partial^2 \widetilde{\phi}}{\partial x^2}\right)
\end{aligned} \tag{2}$$

where the wave breaking turbulent viscosity $\nu_B(x,t)$ is given by

$$\nu_B(x,t) = \begin{cases} \nu_{B0}, & x \in D_b \\ 0, & \text{otherwise.} \end{cases} \tag{3}$$

D_b is the region where the dissipation is applied. The extent of the region is defined by two parameters α and $SlopeB$. The limiting crest front steepness above which the wave is considered to be breaking is represented by $SlopeB = \partial\eta/\partial x$. The upstream extent of the dissipation zone is then calculated as a fraction α of this limiting wave crest front steepness. This is illustrated in Fig. 1. The selection of the parameters used in the dissipation model are discussed in Section 3.4. A detailed analysis of the breaking wave model for different sea states is presented by Wang et al. [39].

2.2. ALE kinematic description and Morison equation

The description of Arbitrary Lagrangian–Eulerian (ALE) method presented by Donea et al. [28] is followed in this study for the kinematic description of the fluid domain on a moving grid. The fundamental ALE equation describes the relationship between the particle or total time derivatives and the referential or local time derivatives. The Reynolds transport theorem that relates the Lagrangian and Eulerian systems can written in differential form as:

$$\frac{df}{dt} = \frac{\partial f}{\partial t} + \vec{v} \cdot \nabla f \tag{4}$$

where f is any parameter, $\vec{v}$ is the particle velocity and the transformation from the Lagrangian to an ALE system can be similarly written as:

$$\left.\frac{\partial f}{\partial t}\right|_{\vec{x}} = \left.\frac{\partial f}{\partial t}\right|_{\vec{\chi}} + \vec{c} \cdot \frac{\partial f}{\partial \vec{x}}\,. \tag{5}$$

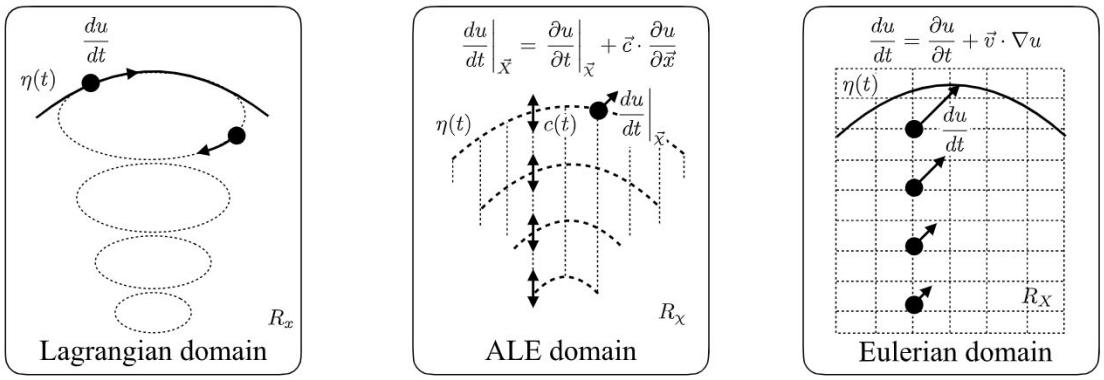

Fig. 2. Flowchart illustrating the transformations between the different coordinate systems.

where $\vec{\chi}$ is the ALE coordinate and $\vec{c}$ is the relative velocity between the particle and the mesh velocity:

$$\vec{c} = \vec{v} - \vec{\upsilon} = \frac{\partial \vec{x}}{\partial \vec{\chi}} \cdot \vec{w} \tag{6}$$

where $\vec{\upsilon}$ is the mesh velocity of the coordinate system. Using Eq. (5), the total derivative of any variable f in an ALE representation can be defined, such as the particle acceleration ($\vec{a} = d\vec{v}/\mathrm{dt}$) in an ALE system is:

$$\vec{a} = \left.\frac{\partial \vec{v}}{\partial t}\right|_{\vec{\chi}} + \vec{c}\cdot\frac{\partial \vec{v}}{\partial \vec{x}} \tag{7}$$

where the convective derivative ($\nabla\vec{v} = \frac{\partial \vec{v}}{\partial \vec{x}}$) is usually calculated in the Eulerian system ($\vec{x}$)(see Fig. 2). .

The modified Morison equation uses the horizontal particle acceleration, which can be estimated in the ALE system for a two-dimensional case using Eq. (7):

$$a_x = \left.\frac{\partial u}{\partial t}\right|_{\vec{\sigma}} + \vec{c}\cdot\frac{\partial u}{\partial \vec{x}} = \left.\frac{\partial u}{\partial t}\right|_{\vec{\sigma}} + \begin{bmatrix} c_x \\ c_z \end{bmatrix} \cdot \begin{bmatrix} \frac{\partial u}{\partial x} \\ \frac{\partial u}{\partial z} \end{bmatrix} = \left.\frac{\partial u}{\partial t}\right|_{\vec{\sigma}} + c_x\frac{\partial u}{\partial x} + c_z\frac{\partial u}{\partial z} \tag{8}$$

which can be reformulated using the definition of the convective velocity and the chain rule for differentiation to:

$$a_x = \left.\frac{\partial u}{\partial t}\right|_{\vec{\sigma}} + u\left(\frac{\partial u}{\partial \xi} + \frac{\partial u}{\partial \sigma}\frac{\partial \sigma}{\partial x}\right) + \left(w - \sigma\left.\frac{\partial \eta(x,t)}{\partial t}\right|_{\vec{x}}\right)\frac{\partial u}{\partial \sigma}\frac{\partial \sigma}{\partial z} \tag{9}$$

where all terms are known or defined in the $\vec{\sigma}$ system.

The incremental horizontal force acting on a strip is defined according to the Morison equation [40] as:

$$\Delta F_x = C_M a_x \rho \Delta V + C_D u|u| \frac{1}{2}\rho \Delta A = C_M a_x \rho A_{xy} \Delta z + C_D u|u| \frac{1}{2}\rho B_p \Delta z \tag{10}$$

where C_M is the inertia coefficient, $\Delta V = A_{xy}\Delta z$ is the volume of the strip (with the cross sectional area A_{xy}), C_D is drag coefficient, ΔA is the projection area, with the section breadth B_p and strip thickness Δz. By integration over the wetted portion of an object, the global horizontal force is defined as:

$$F_x = \lim_{\Delta z \to 0} \sum \Delta F_x = \int_0^{\eta(x,t)} C_M a_x \rho A_{xy} dz + \int_0^{\eta(x,t)} C_D u|u| \frac{1}{2}\rho B_p dz \tag{11}$$

which can be estimated in the $\vec{\sigma}$ coordinate system as:

$$F_x = \rho(h + \eta(x,t)) \left[\int_0^1 C_M a_x A_{xy} d\sigma + \int_0^1 C_D u|u| \frac{1}{2} B_p d\sigma\right] \tag{12}$$

The incremental pitch moment is defined using strip theory as:

$$\Delta M_y = \Delta F_x (z + h) = C_M a_x \rho A_{xy} (z + h) \Delta z + C_D u|u| \frac{1}{2}\rho B_p (z + h) \Delta z \tag{13}$$

which yields the global pitch moment defined in the ALE system:

$$M_y = \rho(h + \eta(x,t))^2 \left[\int_0^1 C_M a_x A_{xy} \sigma d\sigma + \int_0^1 C_D u|u| \frac{1}{2} B_p \sigma d\sigma\right] . \tag{14}$$

The main advantages of the using the Morison equation with ALE strips are:

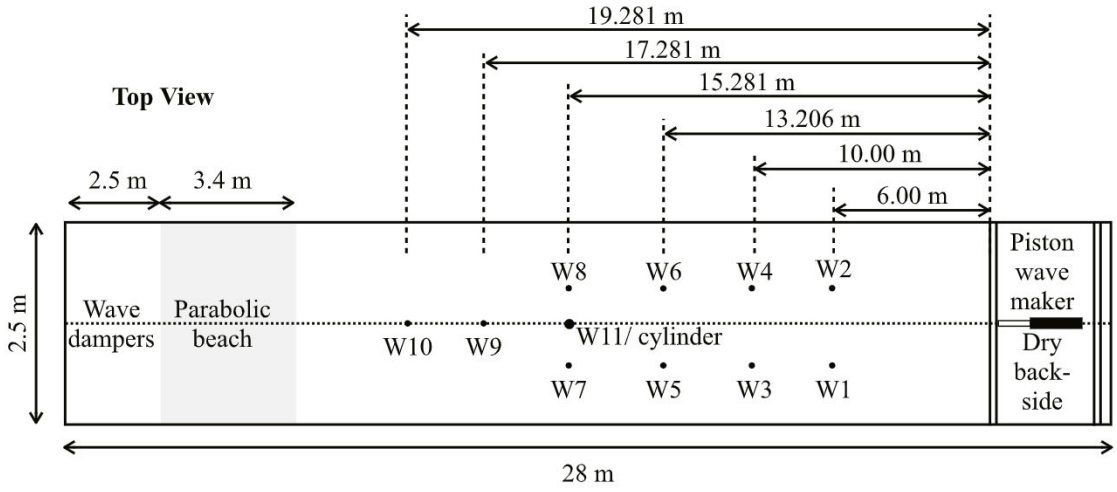

Fig. 3. Small towing tank.

Table 1
Main parameters of the investigated sea states in model scale.

Wave type	H_s (m)	T_p (s)	k_pa	k_ph	$\omega_p^2 h/g$	H_s/h
Regular	0.1375	1.4270	0.136	1.069	1.066	0.25
Jonsawp ($\gamma = 3.2$)	0.1720	1.5556	0.143	0.896	0.898	0.32
Focused ($\gamma = 3.3$)	0.230	1.64	0.197	0.995	0.755	0.455

- As all strips are always under water, the wetted volume need not be explicitly calculated depending on the location of the free surface as in the case of Eulerian strips
- Forces and moments can be directly calculated from the numerical results without any interpolation to a fixed Eulerian frame.

2.3. Model test

The validation of the method uses a model test campaign executed by NTNU and SINTEF Ocean during the [41] project at NTNU/SINTEF Ocean towing tank. The model tests are carried out at a Froude scale of 1:50 [42,43]. The tank is equipped with a piston wavemaker and a towing carriage. At the other end of the tank is a beach with an adjustable height depending on the water depth. The towing tank is 28 m long and 2.5 m wide with a possible water depth between 0 and 1.0 m at model scale. The coordinate system is a right-handed system centred at the seabed at the mean position of the wavemaker. The positive x-axis points in the direction of wave propagation and the positive z-axis points upwards. The model setup is shown in Fig. 3.

The free surface elevation is measured at 11 different locations, where the mono pile is located at the 11th location and is denoted with a solid circle in Fig. 3. The free surface, flap position, temperature, and load signals are sampled at 200 Hz (model scale) with Butterworth filter at 20 Hz (model scale). In this study, measurements from one of the steepest regular waves along with one irregular sea state are used. The water depth in these cases is h =27 m which corresponds to h =0.54 m in model scale. The main parameters of the investigations are listed in Table 1, with all values given in model scale. In the case of irregular waves, the parameters relate to the significant wave height H_s and peak period T_p.

At model scale, a 0.18 m diameter mono pile is modelled by a segmented cylinder with an inner core that ensures the model can be considered to be stiff. The model natural frequency in water is around 24 Hz. This is approximately 5 times the highest frequency of interest- 4.74 Hz, which is the fourth harmonic of a wave of period 0.85 s. 3D-printed plastic shells with the correct diameter and roughness are used to model the cylindrical shape of the mono pile. Foundations are installed in a pit in the towing tank, with a 2DOF force transducer at the top measuring the global pitch moment M_y and the global horizontal force F_x. The models are connected to the force transducer using an intermediate connection piece and placed at the bottom of the tank.

In order to demonstrate application to a steeper wave, a model test presented by Zang et al. [44] is simulated. The non-breaking wave event is generated by a NewWave-type unidirectional focused wave group. The physical experiments are carried out in a shallow water basin with a constant water depth of d = 0.505 m and the cylinder of diameter D = 0.25 m is located at 7.8 m from the paddles in the centre of the tank. The parameters of the focused wave group are presented in Table 1, the parameters are based on the focused wave height H_f.

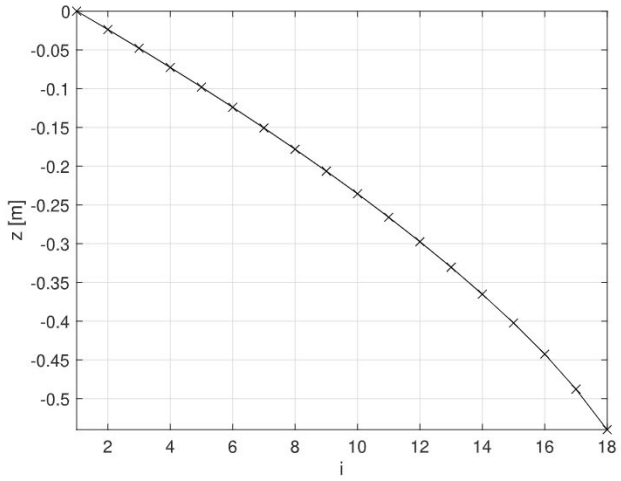

Fig. 4. Vertical distribution of the $\vec{\sigma}$ grid for $d = 0.54$ m.

Table 2
Main wave components of the irregular sea state.

	Shortest wave	Peak period wave	Longest wave
T [s]	0.675	1.56	2.35
f [Hz]	1.482	0.64	0.425
L [m]	0.71	3.16	5.05
C_{ph} [m/s]	1.05	2.03	2.25

2.4. Numerical simulation setup

The numerical domain used in the REEF3D::FNPF simulations is identical to the experimental setup with Dirichlet boundary condition for wave generation and active wave absorption method for wave absorption at the end of the domain. The number and distribution of vertical grids has a significant effect on wave dispersion in a numerical simulation using the Laplace equations [27]. Pákozdi et al. [45] have shown that a minimum of 35 grids per wavelength ($dx = \lambda/35$) is necessary in the model for the satisfactory representation of regular waves along with a method to calculate the optimum vertical grid distribution for a given wave period. Based on these considerations, the optimal vertical grid distribution chosen for the simulations with regular waves is shown in Fig. 4 for $d = 0.54$ m and the number of the vertical grids is chosen to be 18.

The number and distribution of grids for irregular wave simulations is also determined in a similar manner. Three periods are identified to define the grid size and the time step — the shortest wave period, the peak wave period and the longest wave period. The wavelength of the shortest wave, which has the lowest phase velocity defines the horizontal grid size according to $dx = \lambda/35$. The phase velocity (C_{ph}) of the longest wave defines the time step: $dt = dx/C_{ph}$, based on the values presented in Table 2. The location of these periods relative to the wave power spectrum is shown in Fig. 5(a). The wave period of the shortest wave corresponds to the limit of the wavemaker. The period of longest wave is defined at the period where the energy of the JONSWAP spectrum is about 1% of the maximum energy level. The vertical grid distribution is chosen to be close to the optimal distribution for all three waves. The optimal vertical grid distribution for each of the three wave periods is labelled as T_{short}, T_{peak} and T_{long} in Fig. 5(b). The chosen distribution and number of vertical grid points corresponds to that for the shortest waves, which is seen to be 33 in the figure. Wave generation in the simulations is carried out using the measured piston motion as input. The free surface elevation is calculated in the simulations at the same distances from the wavemaker as in the model test enabling a deterministic and direct comparison between the model test and the numerical simulations.

2.4.1. Focused wave simulation

The numerical setup is similar to the above presented setup. In the absence of wavemaker motion, the in-built NewWave-type focused wave group function is used with the Dirichlet boundary condition at the inlet [46]. The grid resolution is chosen following the previously described procedure for irregular waves with 10 vertical grid points. This procedure yields a horizontal grid size $dx = 0.0225$ m, time step $dt = 0.005$ s and a stretching factor $\delta = 1.65$. The length of the numerical domain L is 22.5 m and the water depth is the same as that in the experiment.

3. Results and discussion

A post-processing procedure to determine the wave forces on a cylinder is developed based on the methods presented in the previous sections. In this section, the verification of the ALE method and the validation of the method to estimate the wave forces

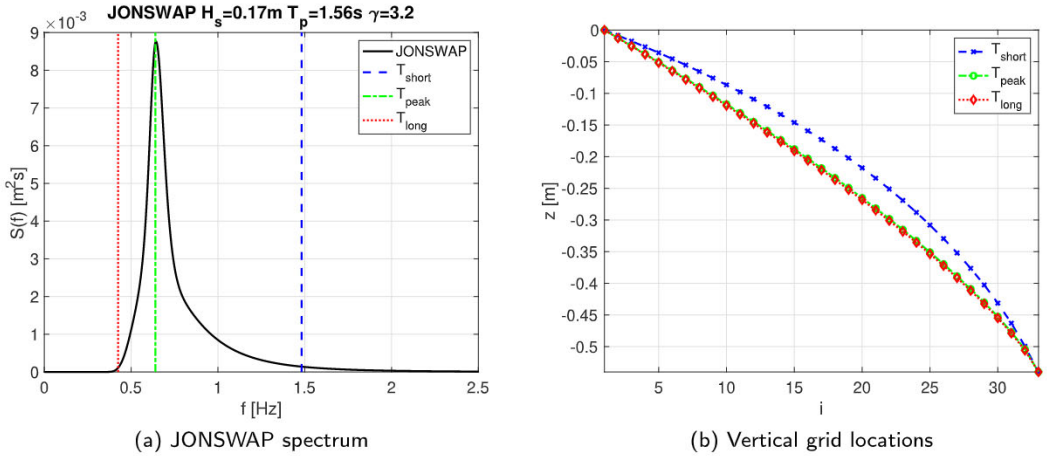

Fig. 5. Representation of the main parameters for the numerical setup and the vertical grid spacing.

on a cylinder in regular and irregular waves is presented. The verification is carried out using the same regular wave as that in the model test described in Table 1.

3.1. Verification of the ALE kinematic method

The method is verified using an example of a regular wave used in the model test. The necessary derivatives are calculated by the finite difference (FD) method, where the coefficients are estimated based on the algorithm presented by [47]. A sixth-order FD scheme is applied to obtain the spatial derivatives and the time derivatives. Since the deformation of the σ-grids is significant for higher wave heights and steepnesses, the difference between the total and the local acceleration will also be significant and the selected regular wave case represents such a case with a wave steepness $k_p a = 0.136$. The fifth-order Stokes wave theory [9] is then used to obtain the theoretical values for the wave kinematic parameters.

The $\vec{\sigma}$-grid for the post processing calculations is defined such that σ is predefined and the vertical coordinates z are calculated according to the analytical solution of the instantaneous free surface position. Fenton's solution for the velocity potential ϕ, its time derivative for the velocity components u, w and the acceleration components a_x, a_z are calculated at the grid locations over several time steps. The number of time steps is defined by the truncation order $O()$ of the finite difference scheme and the sixth-order scheme used in this study yields seven time steps. The time step size is defined from the wave phase velocity: $dt = 0.1\lambda/T$, the number of grids in the $x-$ and $z-$ directions are $N_x = \lambda/64$ and $N_z = 16$ respectively and the grids are uniformly distributed in both the directions.

The horizontal and vertical velocity field for the regular wave is shown on the σ-grid for time $t = dt(O()/2 + 1)$ in Fig. 6. As a sixth-order FD scheme is used to estimate the spatial derivatives, seven horizontal fixed locations are needed at each vertical location of the σ grid to calculate the horizontal derivatives $\partial/\partial x$ in the Eulerian system. These locations define an orthogonal grid, represented as black circles in Fig. 6. The highest coordinate of the black circles is chosen such that all fixed points are always under the free surface and the fourth location coincides with the σ-grid points. The total time derivatives of ϕ, u, w are calculated using the Reynolds transport theorem in Eq. (5) at the location where the black circles coincide with the σ grid. Similarly, the parameters ϕ, u, w determined from the analytical solution are compared to those calculated using the ALE framework. The verification of the spatial derivatives, time derivatives and the total derivatives at chosen locations is presented below.

3.1.1. Verification of the spatial derivatives

The verification of the spatial derivatives is presented in Fig. 7. The red lines with cross markers show the absolute error in the estimation of the spatial derivatives from the circles shown in Fig. 6. The black lines with circle markers show the absolute error of the spatial derivatives which are calculated on the $\vec{\sigma}$ system. The spatial derivatives of ϕ $(\partial\phi/\partial x, \partial\phi/\partial z)$ calculated using the sixth-order finite difference scheme are compared with the analytical solution for the velocity (u, w) from the fifth-order Stokes theory in the upper diagrams. The spatial derivatives of $\partial\phi/\partial t$ are compared with the acceleration based on Fenton's model in the lower diagrams. For the $x-$ derivative only the central difference scheme is used as sufficient grid points are always available. Therefore, the calculated errors are smooth in the vertical direction. On the other hand, vertical derivatives are estimated at both ends either by the forward and backward scheme and by the central scheme otherwise. This results in the large gradients at both ends of the curves. In the $\vec{\sigma}$ system, when the horizontal derivatives are calculated, the vertical derivative over the σ coordinates $\partial/\partial\sigma$ are also involved, leading to more uneven error curves. Due to the several numerical derivations involved, the accuracy of the Euler gradients estimated on the σ-grid is less than that for the orthogonal grids. However, based on the low values of the errors, it can be concluded that the numerical implementation is correct and consistent with the analytical results for the velocity potential and its time derivatives — velocity and acceleration.

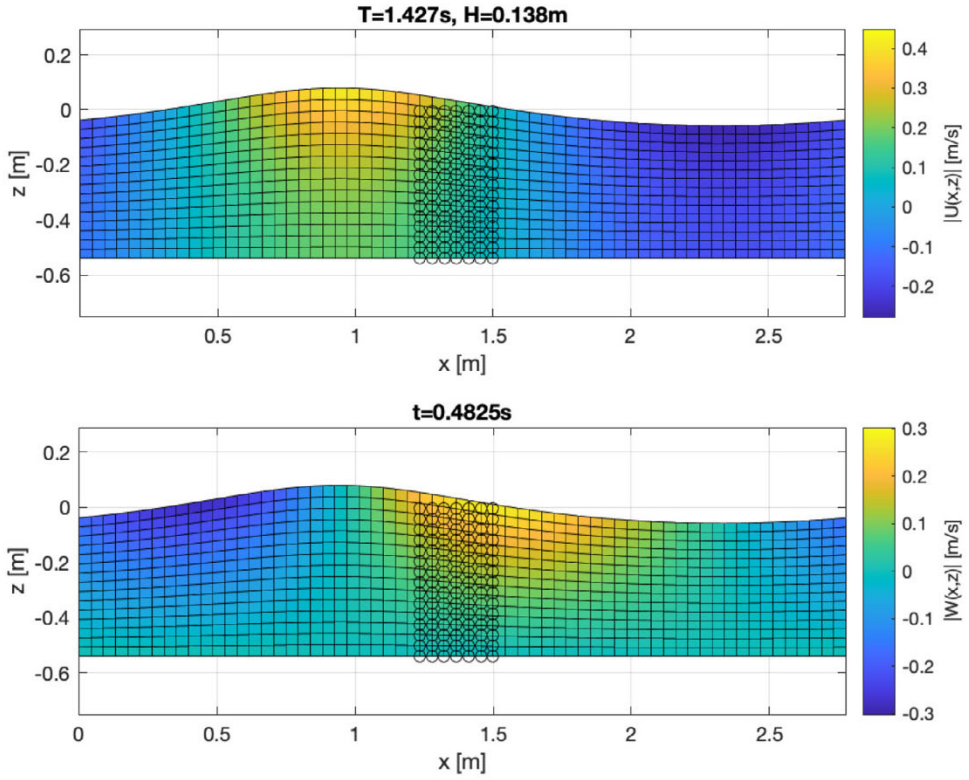

Fig. 6. The velocity components of the 5th-order Stokes wave.

3.1.2. Verification of the local time derivatives

The sixth-order central difference scheme is used to estimate the local time derivatives. The parameters are estimated by the Fenton's model at seven different time points. The time derivatives are estimated at the fourth time point at the coinciding points in the diagrams presented in Fig. 8. The upper right hand side diagrams show the comparison of $\partial\eta/\partial t$ and $\partial z(\sigma)/\partial t$ using the deformation velocity of the grid $\sigma\partial\eta/\partial t = \partial z(\sigma)/\partial t$. All diagrams show that the finite difference scheme is very accurate even over a small time step.

3.1.3. Verification of the total time derivatives

The total time derivatives are calculated in the Eulerian system and compared to the total derivatives estimated in the ALE $\vec{\sigma}$ system. The errors are found to be lower than the perturbation error of the fifth-order Stokes wave theory, $k_p a^6 = 1.4138 \cdot 10^{-5}$ as shown in Fig. 9.

3.2. Validation of the estimated forces due to a regular wave

In this section, the procedure is validated using the measured results for the free surface elevation, global forces and moments on the structure from the regular wave case in the model test. The comparison of the measured and numerically estimated time series of the free surface elevations is presented in Fig. 10 for six different locations. There are minor differences between the measured and calculated free surface elevations, but the agreement can be termed sufficient for the validation of the hydrodynamic loads.

In Fig. 11, a part of the numerical domain is shown at two different time instances. The left hand side diagrams present the $\vec{\sigma}$ framework with the values of the horizontal velocity as well as the σ-grid where the time series of the horizontal total acceleration and the horizontal velocity are estimated for the location 15.218 m from the wavemaker. This is also the location of the mono-pile where the hydrodynamic loads are measured in the presence of the structure. The right hand side diagrams show the numerical domain with the horizontal velocity and the physical location of the fluid with the numerical grid.

Applying (9) to the σ-grid, the total horizontal acceleration is defined at all grid points. With the help of a spline function, these values, a_c and u are interpolated to the location of interest: $\xi = 15.218$ m for all σ positions. The result of these procedures with the instantaneous z-coordinates is shown in Fig. 12 for the two time instances presented in Fig. 11. The curves show a smooth spatial profile. This procedure is followed for each numerical time step to obtain time series of the instantaneous z-coordinates, the total horizontal acceleration a_x and the horizontal velocity at the predefined σ values as shown in Fig. 13. The free surface location at $\sigma = 1.0$ and the bottom at $\sigma = 0.0$ are seen in the upper diagram. The increase in the magnitude of the parameters with increasing

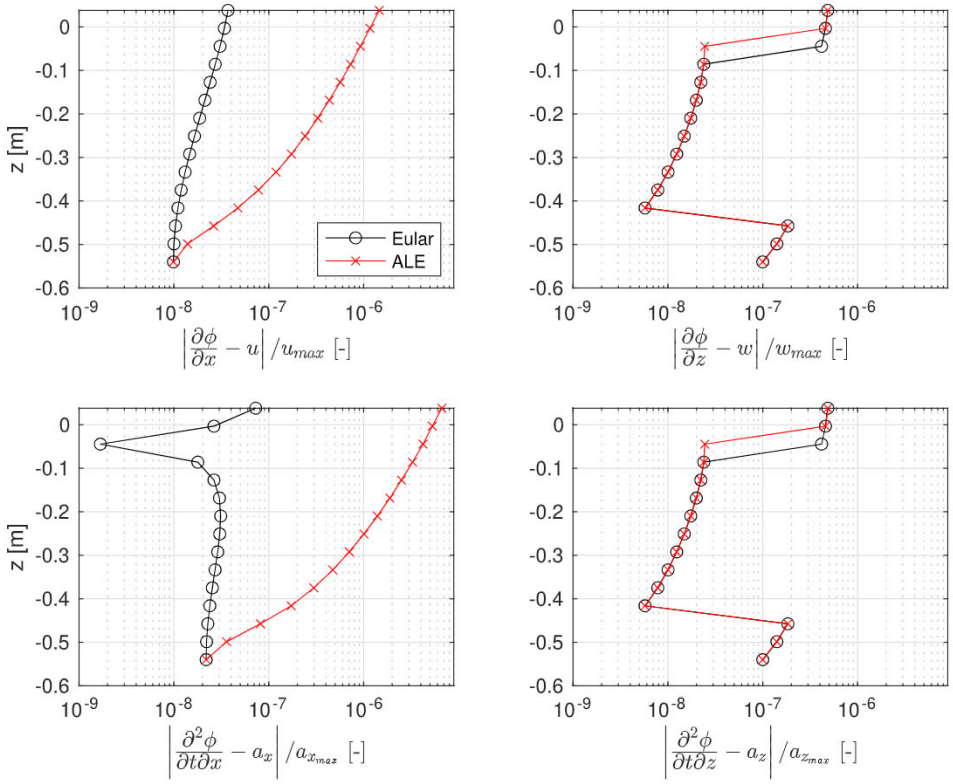

Fig. 7. Relative error in the calculation of spatial derivatives.

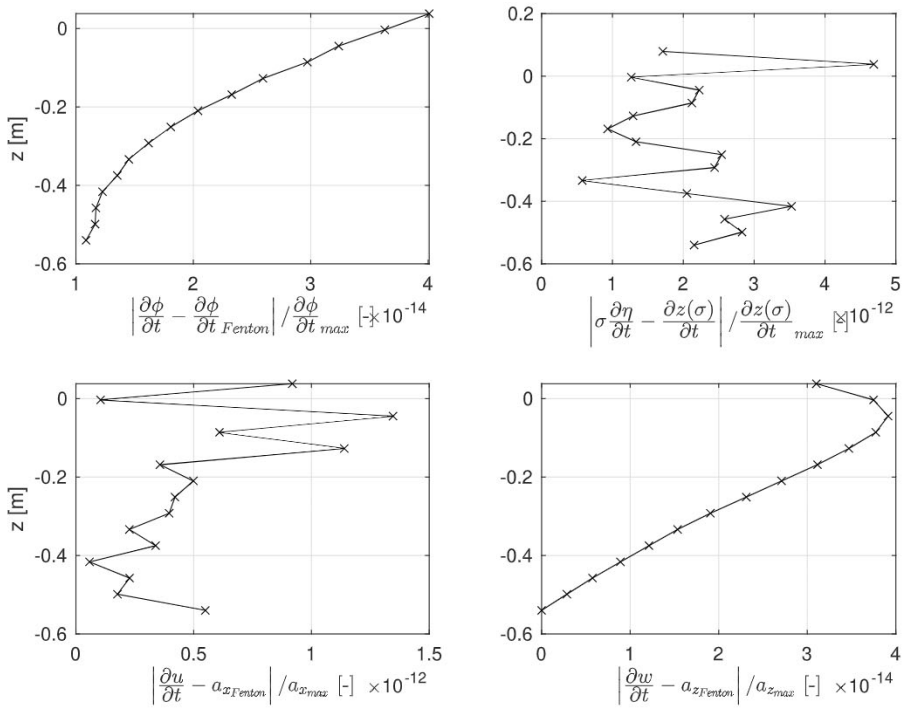

Fig. 8. Relative error in the calculation of local time derivatives.

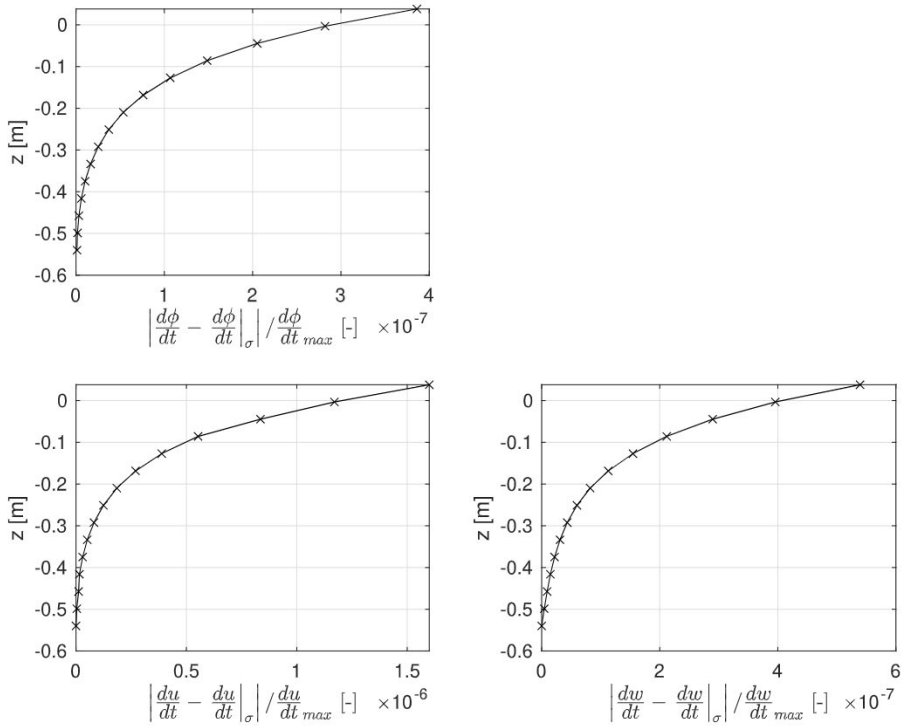

Fig. 9. Relative error in the calculation of total time derivatives.

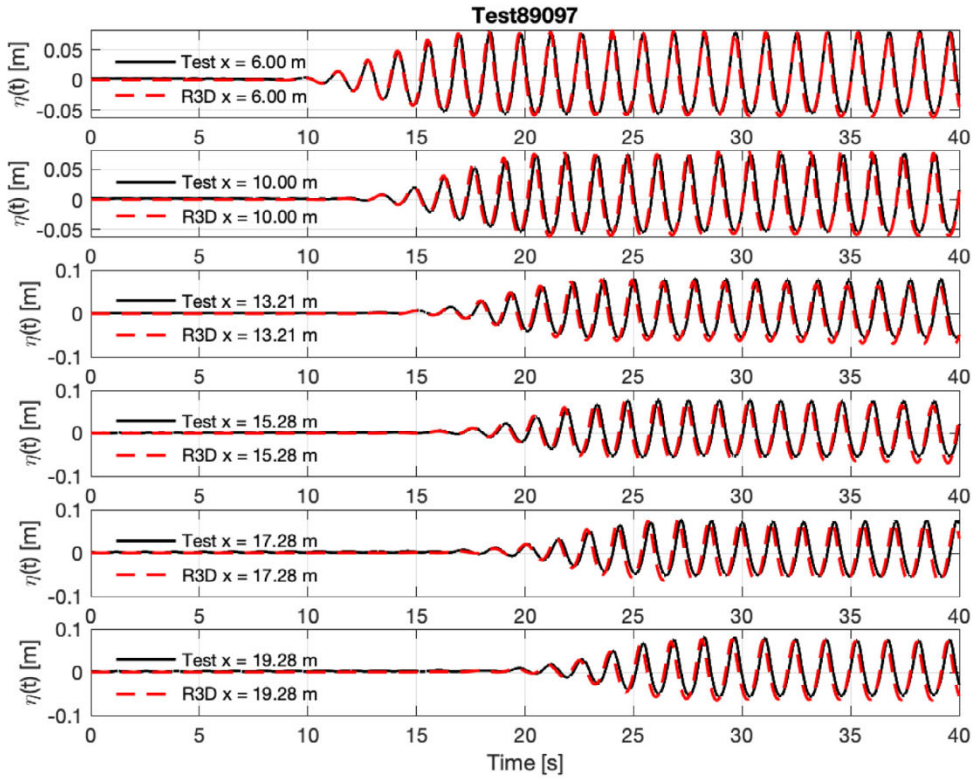

Fig. 10. Comparison of the numerical and measured free surface elevation for regular waves with $T = 1.427$ s, $H = 0.1375$ m.

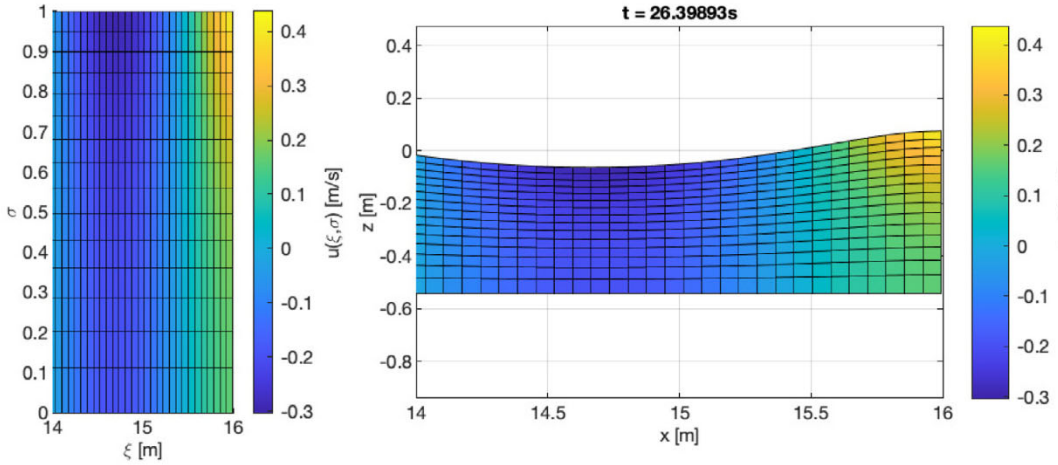

(a) REEF3D::FNPF $t = 26.40\,\mathrm{s}$

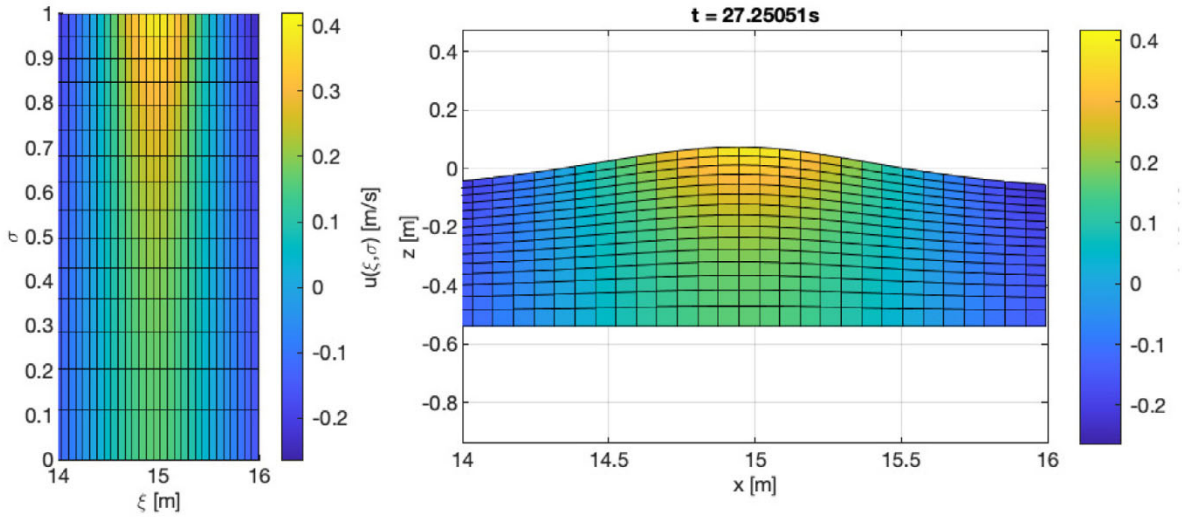

(b) REEF3D::FNPF $t = 27.25\,\mathrm{s}$

Fig. 11. Numerical domain at two different time instances.

vertical location is also seen. The time series of the horizontal velocity and acceleration are smooth, as they continuously include the velocity and acceleration at the free surface ($\sigma = 1.0$). Since the velocity is not measured in the model tests, the validation of these curves is only possible indirectly, through the measured global horizontal forces F_x and global pitch moment M_y.

The forces and moments are calculated using (12) and (14) for every time step. The integration is carried out using the Matlab function `mmpint` [48], which integrates a curve based on its cubic spline representation. The integration is split into the inertial forces and moments with the unit inertial coefficient C_M, and the viscous forces and moments with the unit drag coefficient C_D. This allows for straightforward sensitivity analysis of the coefficients.

The numerically estimated hydrodynamic loads, the measured global force and moment as well as the free surface elevations are presented in Fig. 14. The inertia force and moment are calculated using a inertia coefficient $C_M = 2.047$ according to MacCamy and Fuchs [49], with wave number $k = 2.262\,\mathrm{m}^{-1}$ estimated from the fifth-order Stokes wave theory [9] for a wave period $T = 1.42\,\mathrm{s}$ and a wave height $H = 0.137$ m. A drag coefficient $C_D = 0.7$ is chosen following the DNVGL-ST-0437 [50] standard.

The spectral analysis of the free surface shows the first three harmonics, while the fourth and the fifth harmonics are seen in the spectrum of the pitch moment. Small differences are observed between spectral amplitudes of the measured and numerical signals at the second and third harmonics of the force and moment. This is expected from the small differences previously observed in the time series of the free surface elevations in Fig. 10 and is considered to be insignificant.

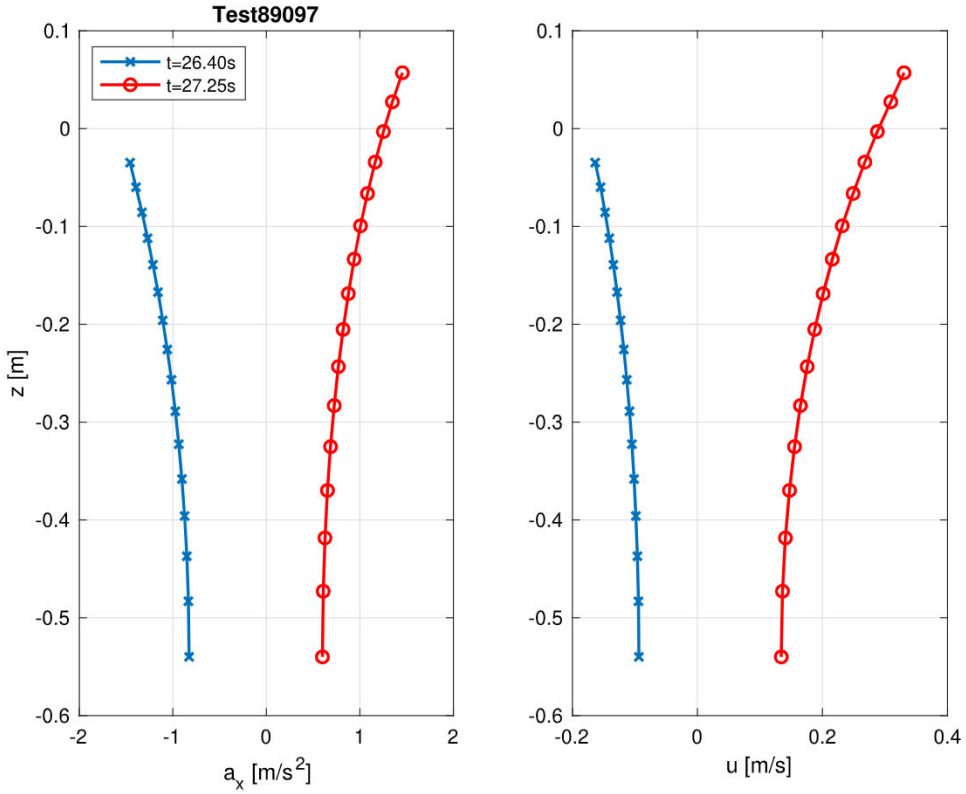

Fig. 12. The horizontal total acceleration and velocity at $x = 15.218$ m at two time instances.

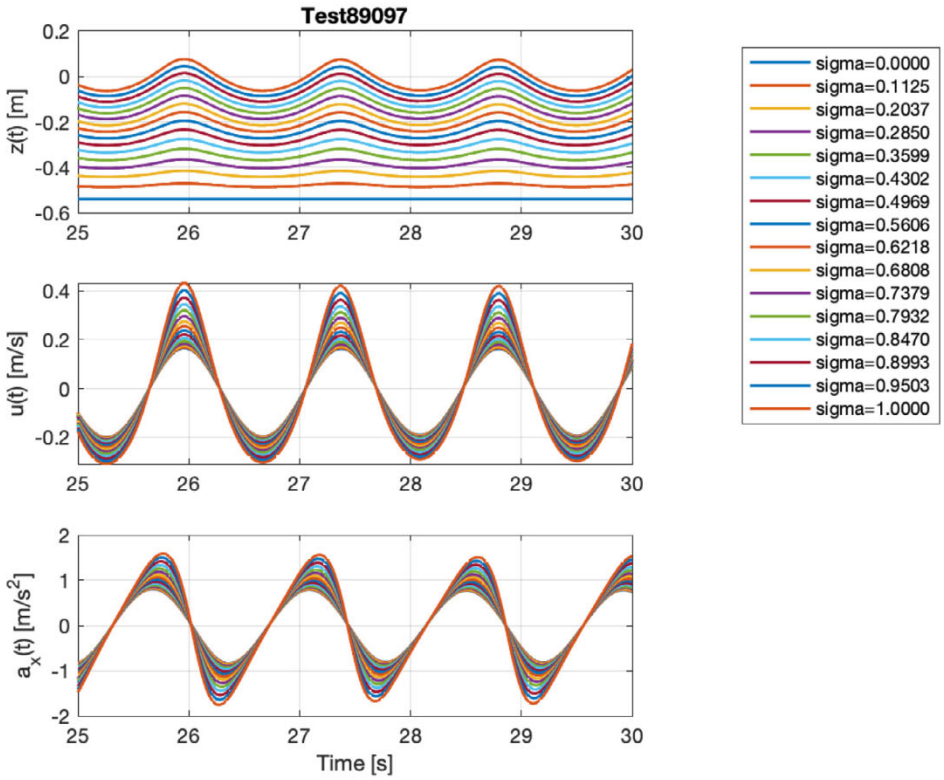

Fig. 13. The estimated time series at $x = 15.218$ m.

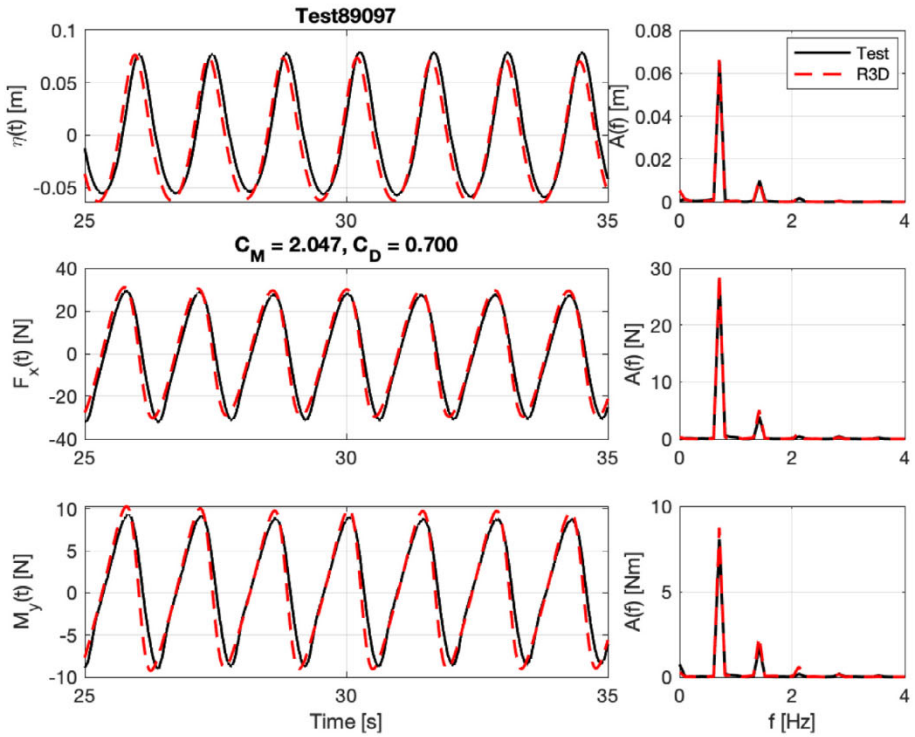

Fig. 14. Validation of the estimated horizontal force and pitch moment acting on the monopile.

3.3. Validation of the estimated forces due to a focused wave group

A focused wave group is simulated to validate the results for the hydrodynamic loads in steep waves. The measured free surface elevation and horizontal force time series are compared with numerical results in Fig. 15. The upper diagram shows a good agreement between the experiment and the simulation for the wave height and wave steepness at the location of the desired focus location and the time. The asymmetrical troughs around the largest wave component in the measured data signifies that the actual location of the focus might be further downstream. Therefore in the simulation, the focus point is defined 1.8 m downstream compared to the experiments. This delays the focus time by 1 s and the simulation yields the unsymmetrical waves troughs around the highest free surface elevation as shown in Fig. 16. The comparison of the force time series shows that not only the free surface elevation but also the numerically estimated wave kinematics are in good agreement with the experiment. The result of the ALE procedure, the total horizontal acceleration a_x with the horizontal velocity at the predefined σ values and with the instantaneous z-coordinates are shown in Fig. 16. It is important to note the smoothness of the acceleration time series, demonstrating the advantage of using a NWT with the ALE procedure to estimate the hydrodynamics load using the Morison equation.

3.4. Validation of the estimated forces due to irregular waves

In this section, an irregular three-hour duration sea state simulation is used to demonstrate the capability and accuracy of the presented ALE-based procedure. The selected sea state consists of several spilling wave breaking events and can demonstrate the robustness of the FNPF model used to generate accurate information about the sea state in an undisturbed condition. Since the sea state consists of wave components beyond the limits of the second-order irregular wave theory, the ALE method to evaluate the wave hydrodynamics is highly relevant in this case. The wave kinematics cannot be determined analytically in this situation and numerical wave tanks are necessary for the calculation of wave kinematics for such steep sea states. The reproduction of the time series of wave elevation by the FNPF model, and the identification and approximation of an extreme event in the sea state using the combination of FNPF modelling and the ALE strategy is demonstrated. Extreme events identified in this manner can then be analysed in a Navier–Stokes equations-based solver.

During the numerical simulations following the parameters listed in Table 1, several wave breaking events are encountered. In order to account for these events, the artificial wave breaking turbulent viscosity parameter $\nu = 1.86$ is used following Baquet et al. [24]. The power spectrum of the free surface elevation measured at the location of the mono-pile $x = 15.218$ m is shown in Fig. 17(a). Using $\nu = 1.86$ resulted in underestimated wave crest height statistics as seen from the curve with the triangular markers in Fig. 17(b). A parametric study of the wave breaking turbulent viscosity is then carried out to identify the value required to obtain

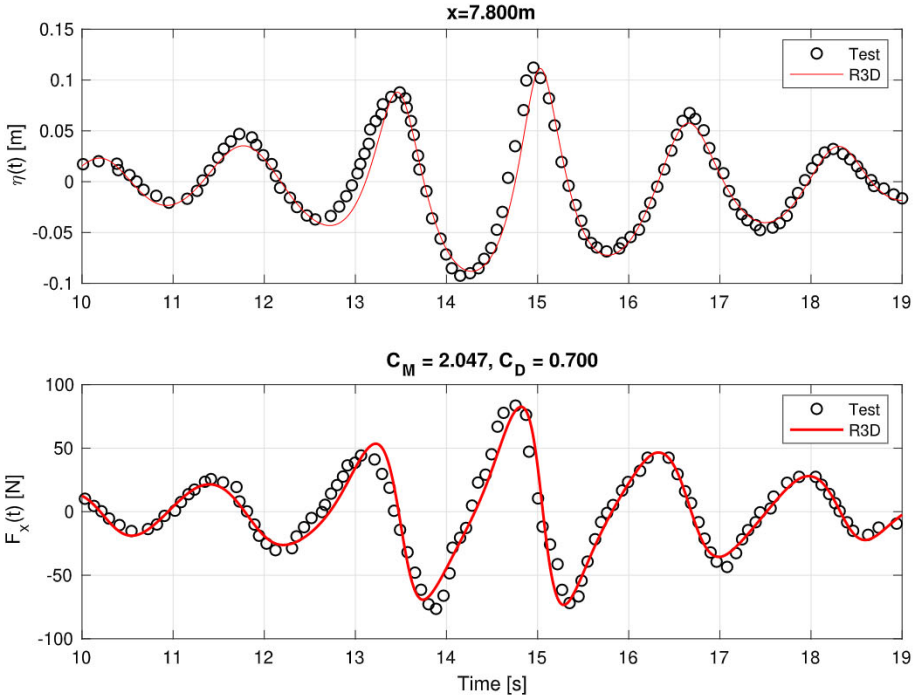

Fig. 15. Validation of the free surface elevation and the estimated horizontal force on the vertical cylinder.

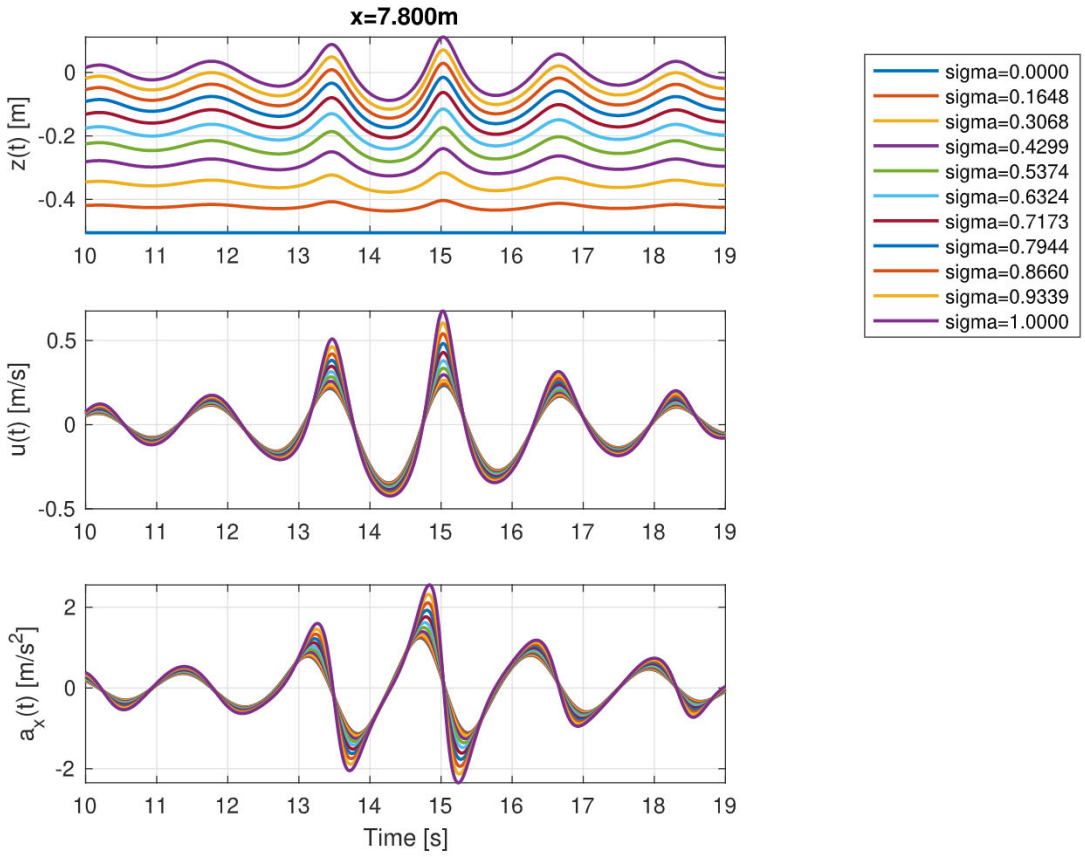

Fig. 16. The estimated time series at $x = 7.8\,\mathrm{m}$.

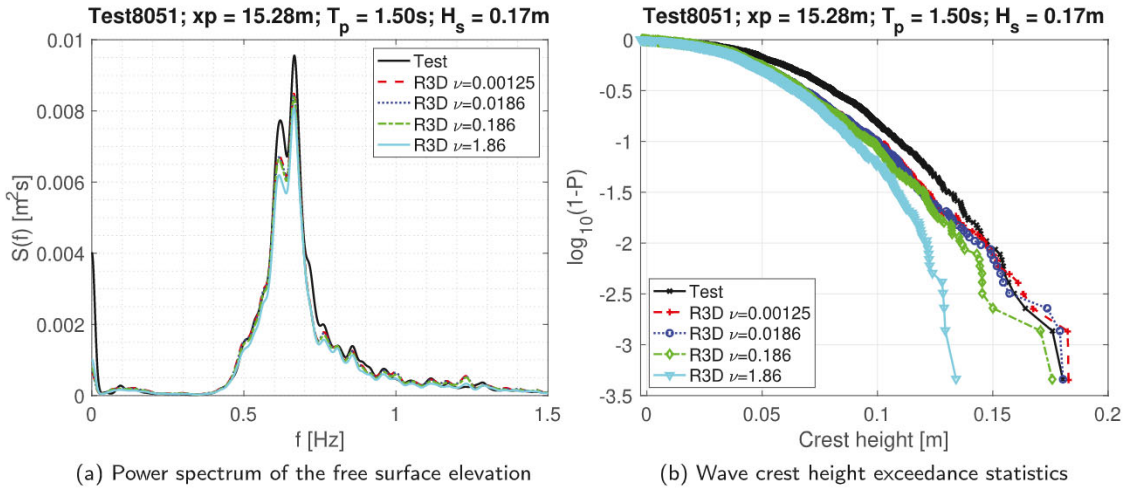

(a) Power spectrum of the free surface elevation (b) Wave crest height exceedance statistics

Fig. 17. Parameter study for the wave breaking turbulent viscosity parameter.

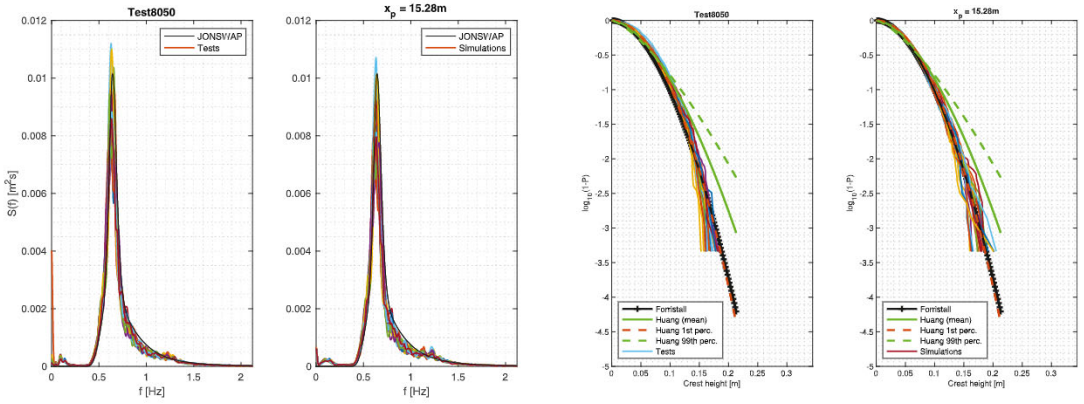

(a) Power spectrum of free surface elevation (b) Wave crest height exceedance statistics

Fig. 18. Power spectrum and crest height statistics of the free surface in model tests and simulations.

similar crest height statistics in the numerical simulation as that measured in the experiments, similar to the parametric approach in Buldakov et al. [51]. The results from the three additional simulations are presented in Fig. 17. The shape of the spectra estimated from the numerical simulations is in good agreement with the measured spectrum. All numerical spectra are slightly lower at the peaks compared to the measured spectrum as previously reported in [52]. It is observed that the viscosity parameter effects the crest height statistics more compared to the power spectrum. The results from the three additional simulations with the lower values for the wave breaking turbulent viscosity parameter are found to be similar for both the power spectrum and the crest height statistics. The peaks of the power spectrum in the simulation with $\nu = 1.86$ are about 10% lower than that in the other simulations, whereas the difference is appreciably higher in the case of the crest height statistics. The best match between the numerical results and the measurements is observed with the factor $\nu = 0.0186$. Following the procedure recommended by Baquet et al. [24], the $\nu = 0.0186$ is chosen as the optimal value. While available results from experiments are used to optimise ν in this case, this can be also determined be determined using CFD simulations in the absence of measured data. In order to further demonstrate the ability of the model to represent sea states with breaking waves, the power spectrum of the free surface elevations from multiple realisations and the wave crest height statistics from an additional model test run with the same input characteristics are presented in Fig. 18. The power spectra from the multiple realisations calculated from the numerical results are within the range of the values calculated from the model tests. The wave crest height exceedance calculated using the simulated free surface compares well with the measured data, as seen from the comparison of each data set with exceedance statistics from Forristall [53] and Huang and Guo [54] in Fig. 18(b).

3.4.1. Validation of the hydrodynamic load statistics

Based on the irregular wave kinematics obtained from the numerical simulation, the global horizontal force and global pitch moment are estimated using the ALE strip theory-based method presented above. The same inertial coefficient $C_M = 2.047$ and drag

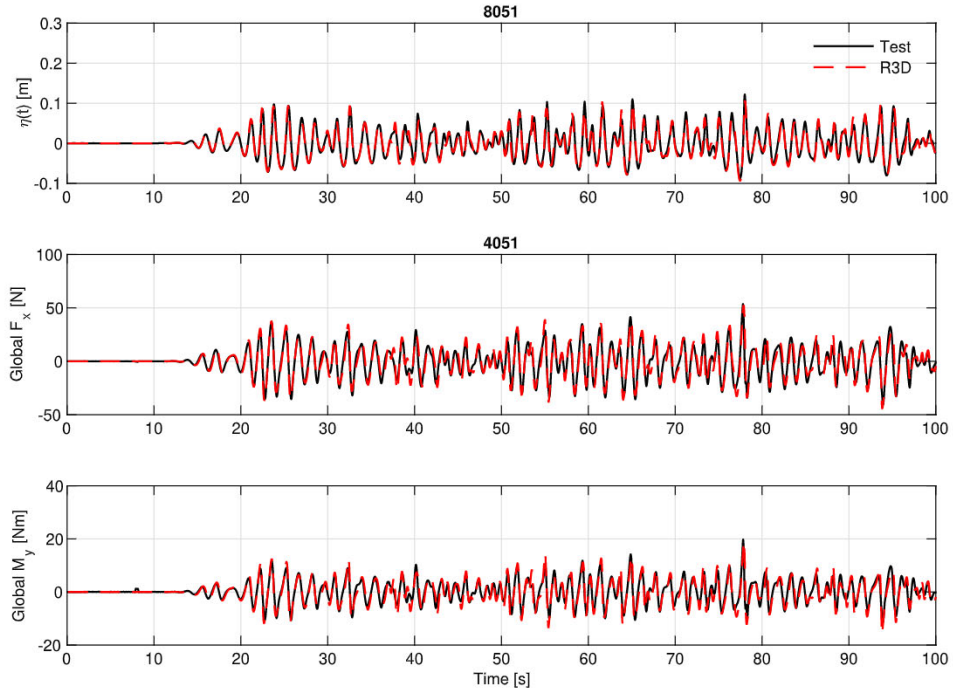

Fig. 19. Comparison of the measured and numerical time series for the free surface elevation, global horizontal force and moment at $x = 15.218$ m for $t = 0-100$ s.

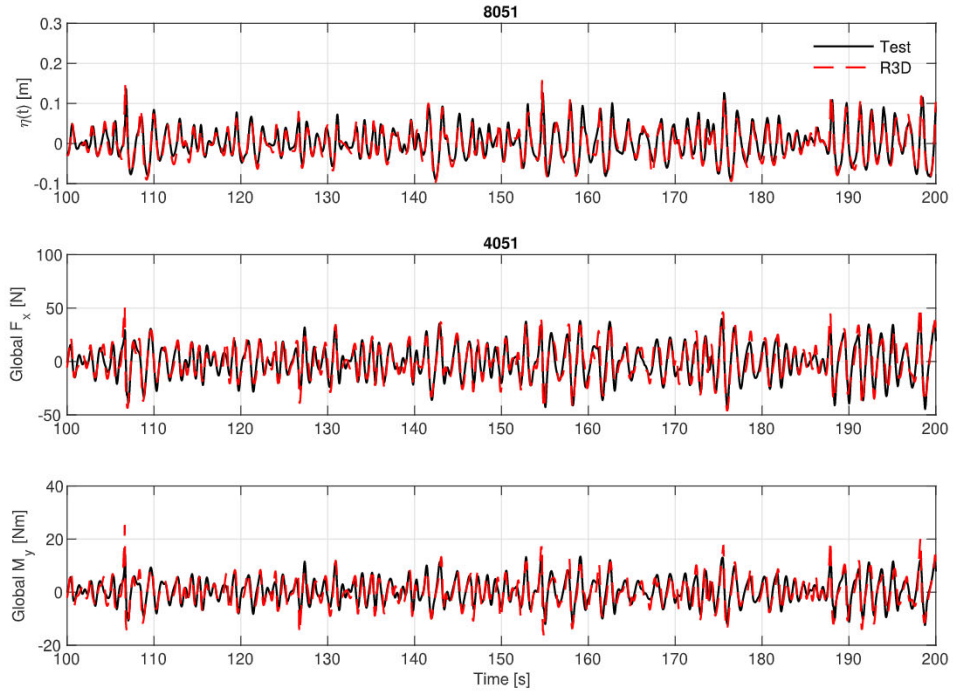

Fig. 20. Comparison of the measured and numerical time series for the free surface elevation, global horizontal force and moment at $x = 15.218$ m for $t = 200-400$ s.

coefficient $C_D = 0.7$ used previously are applied in the Morison equation in Eqs. (12) and (14). The time series of the free surface elevation, the horizontal forces and pitch moment are compared to the measured time series. Figs. 19–21 show the comparison for time intervals $t = 0 - 100$ s, $100 - 200$ s and $200 - 300$ s respectively. The following observations can be made from these results:

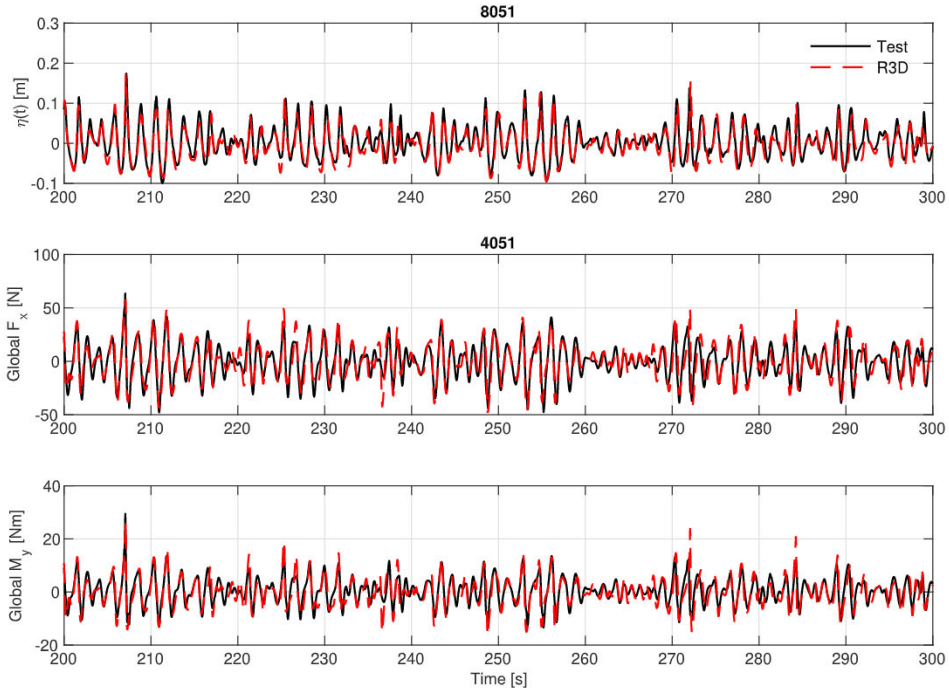

Fig. 21. Comparison of the measured and numerical time series for the free surface elevation, global horizontal force and moment at $x = 15.218$ m for $t = 400-600$ s.

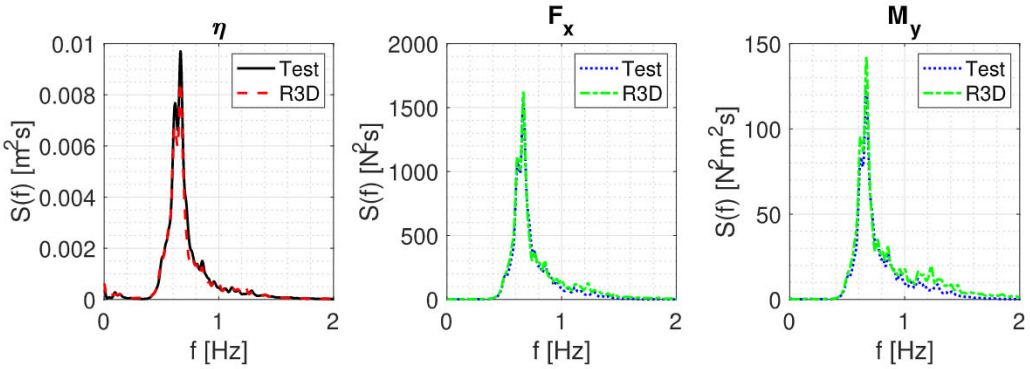

Fig. 22. Comparison of the power spectrum from the measured and computed time series.

- The measured time series of the free surface elevation is slightly higher than in the simulation
- The extremes of the free surface elevations have the same bound but these do not happen at the same time
- The numerical values are higher than the measurements in the case of force and moment time series
- Significantly larger maximum peaks can be observed in the numerical signals without filtering
- The low pass filtered signals for both the measurements and simulations show good agreement

These observations are verified by the power spectrum in Fig. 22 and the exceedance curves in Fig. 23. The two peaks of the free surface power spectrum are higher in the experimental signal and its significant wave height H_s is about 4 percentile higher than the numerical signal (0.1640/0.1572 m). The comparison of the force power spectra shows that the numerical signal has slightly more energy, the significant value of the global horizontal force is about 6% larger than that of the experimental signal (67.81/63.86 N). The power spectra of the global pitch moment show the largest differences between the experiments and the numerical simulation. Values are overestimated at the peaks of the spectrum and the significant value of the numerical signal is 14% higher (21.73/19.09 N m). A higher energy level is identified in the numerical simulations in the frequency range 1.0 Hz to 1.5 Hz. The exceedance of the largest forces and moments show that the maximum values are overestimated in the numerical simulations. An offset of about 15% for the horizontal maximum forces and 25% for the maximum pitch moment curves is observed between the numerical and experimental results.

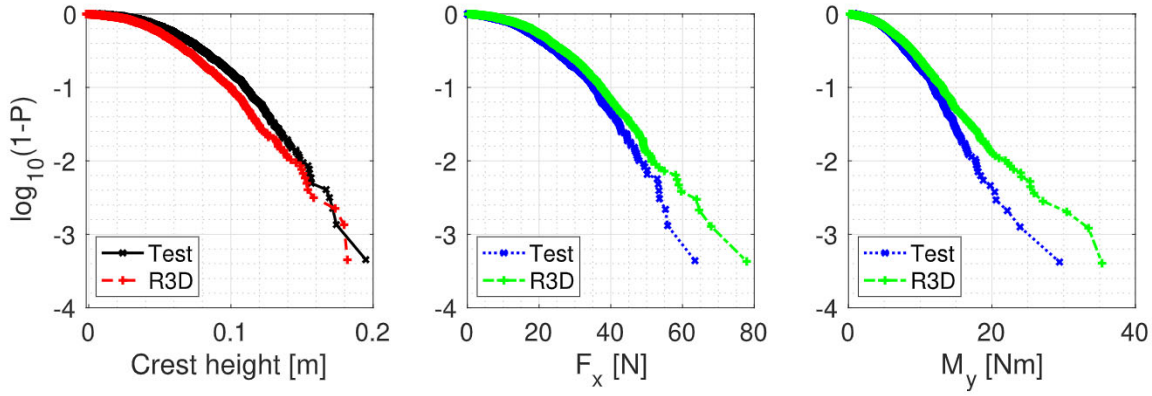

Fig. 23. Comparison of the probability of exceedance calculated from the measured and computed time series.

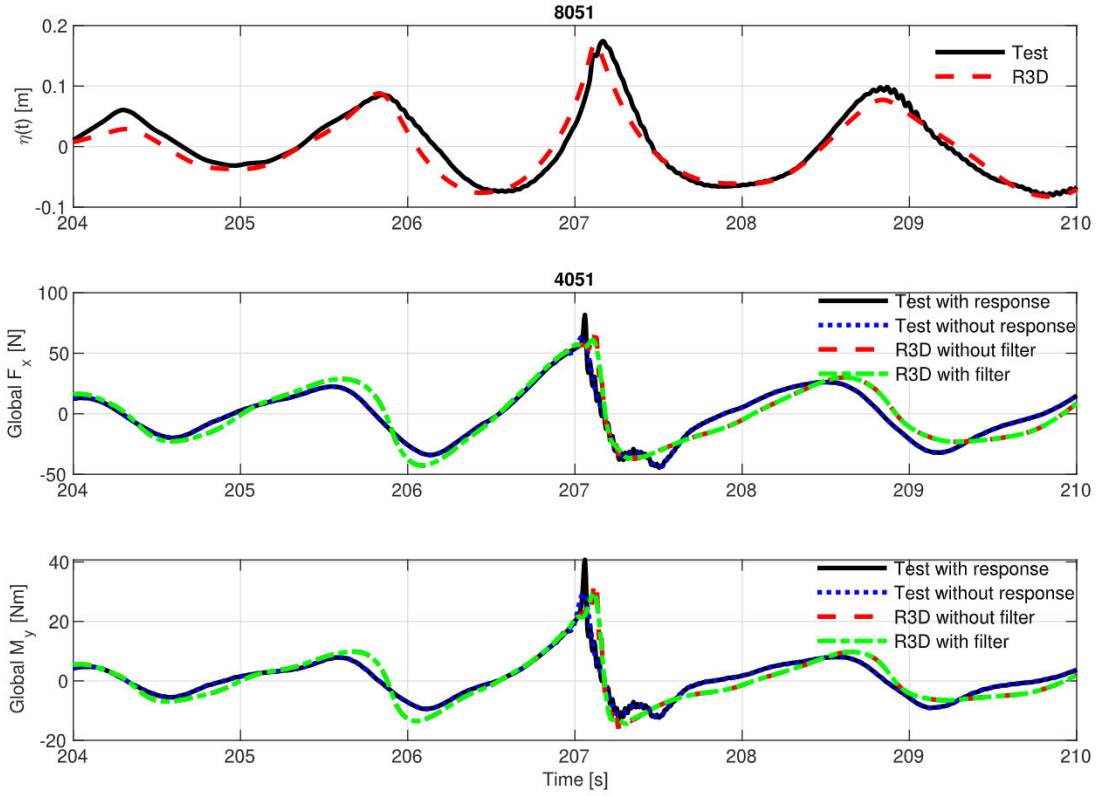

Fig. 24. Measured and treated test data along with computed and filtered time series at $x = 15.218\,\mathrm{m}$.

3.4.2. *Validation of the largest experimental horizontal force event*

The wave event with the largest measured horizontal force is further analysed to discuss the appearance of the unphysical peaks in the numerical simulations. This event is shown in Fig. 24 with a peak in the force and in the moment diagrams. The influence of the measuring instrument on the recorded signals can clearly be seen in the untreated load signals with a high frequency oscillation with a frequency about 24 Hz. The measured force and moment time series are treated using the method presented by Ma et al. [55] to remove the effects due to the excitation due to wave impact. The numerical signal is treated with a low pass filter to remove unphysical peaks seen in the time series. The oscillations in the measured free surface elevation time series with structural response at $t = 207.2\,\mathrm{s}$ indicates spilling wave breaking similar to that reported by Esandi et al. [56]. The crest height and the rise velocity ($d\eta/dt$) of the numerical time series is very similar to the measured values. This indicates that the wave breaking algorithm in the numerical simulation is activated, reducing the wave elevation and the fluid velocity to account for the energy dissipation related to wave breaking. This energy dissipation reflected through the change in the free surface elevation in the simulation results in a

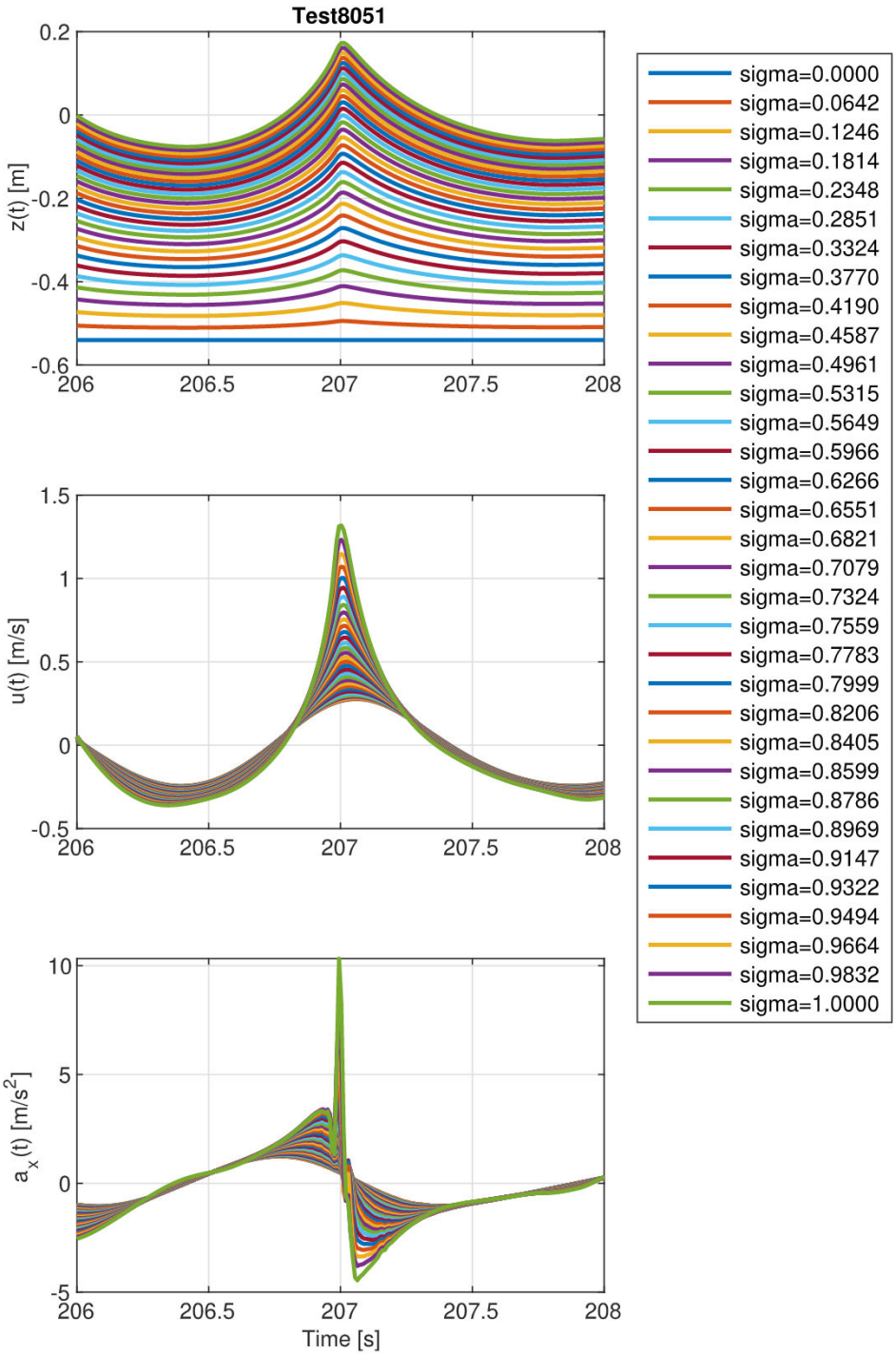

Fig. 25. The estimated time series at $x = 15.218$ m.

sudden change in the calculated total horizontal fluid acceleration as shown in Fig. 25, and is the source of the peaks calculated in the global load curves (green line in Fig. 24). The secondary peaks seen in the force times series which are not represented in the calculated time series arise from higher-order wave–structure interaction. These cannot be reproduced with the current method as the undisturbed wave kinematics are used. The results show that the physical effects of wave breaking are sufficiently represented by the dissipation parameter in the numerical simulations, as otherwise, the calculated peak would be unreasonably high. In these simulations, the peaks are of a reasonable magnitude and are interpreted as an unphysical artefact of representing wave breaking

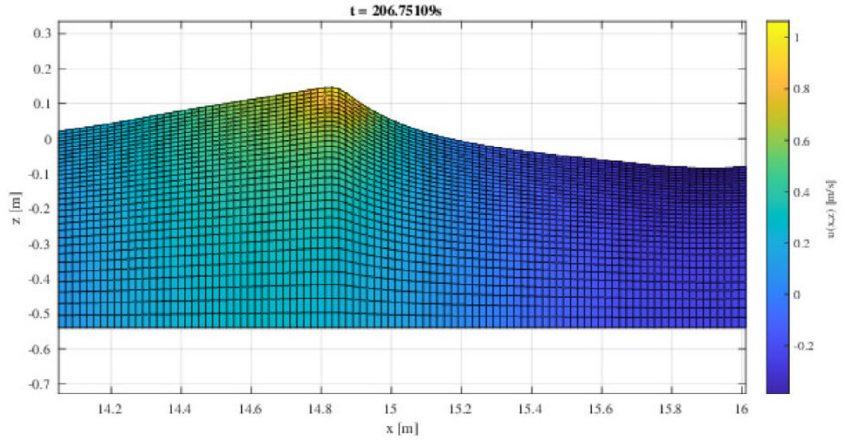

(a) $t = 206.75$ s

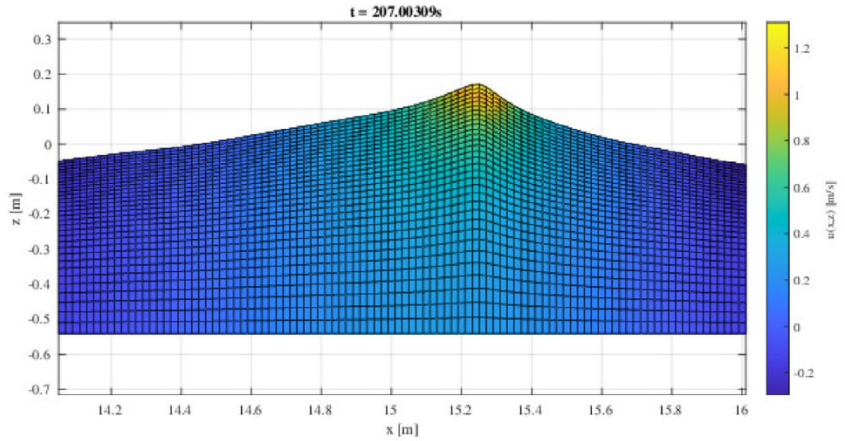

(b) $t = 207.00$ s

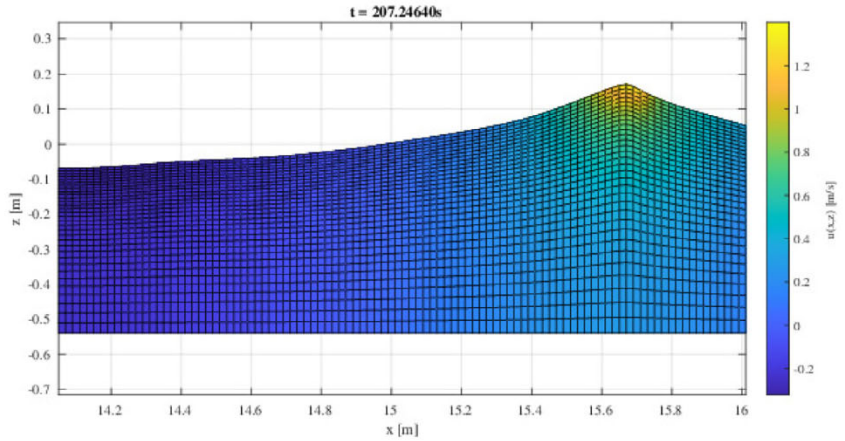

(c) $t = 207.25$ s

Fig. 26. Numerical domains in REEF3D::FNPF at three different time instances.

in a Laplace equation-based model and are removed with the help of a low-pass filter. The resulting curves (red lines) show good agreement with the experimental load histories without response (blue line). The choice of the cut-off frequency of the low pass filter influences the maximum value of the load curves and in turn extreme value statistics shown in Fig. 23. Since the breaking wave energy dissipation mechanics acts only at the free surface, the spatial solution of the Laplace equation is smooth for the distribution

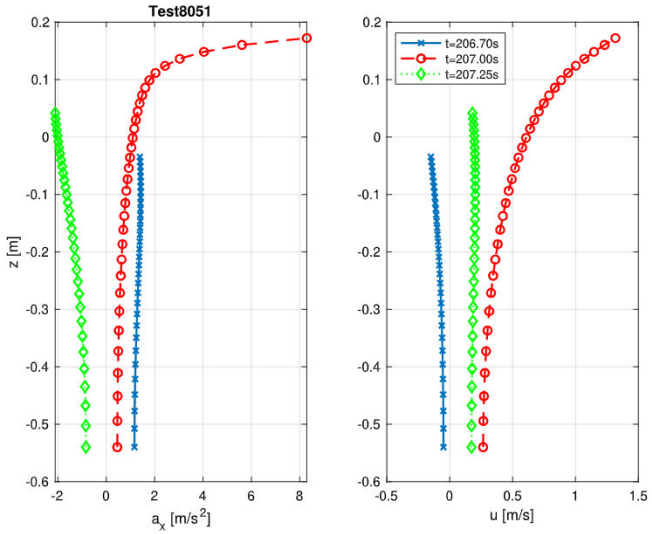

Fig. 27. Calculated total horizontal acceleration and velocity at $x = 15.218$ m at three different time instances.

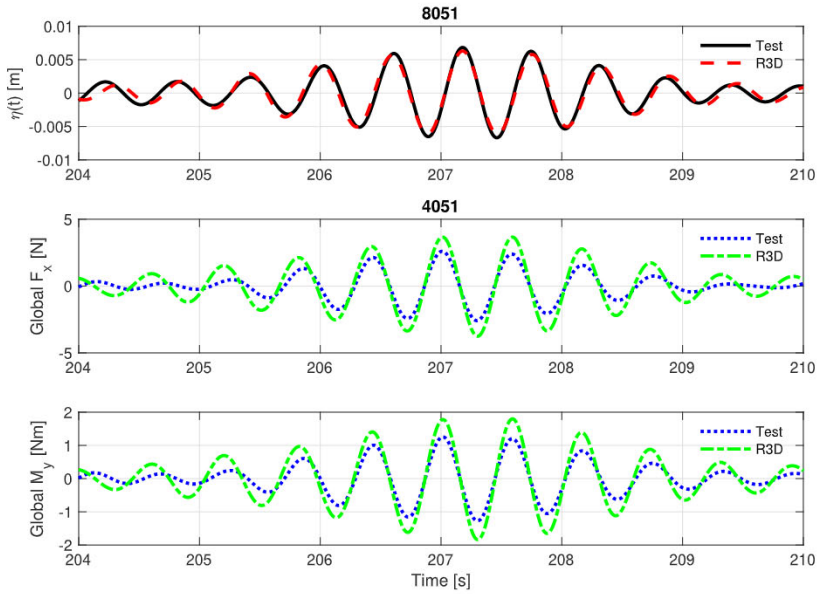

Fig. 28. Band filtered time series at $x = 15.218$ m showing the high frequency components in the free surface elevation, global total forces and moment.

of velocity and acceleration components as shown for three different time steps in Fig. 26. The profiles of the horizontal velocity and acceleration at the same three time steps is also smooth as shown in Fig. 27.

The high frequency component of the calculated and measured wave forces are obtained using a band filter with cut-off low and high-pass frequencies $f_{low} = 1.85$ Hz and $f_{high} = 1.67$ Hz respectively. These forces originate from spilling wave breaking can be responsible for significant response from the structure as reported by Esandi et al. [56]. The same force coefficients as those used above are employed and presented in Fig. 28. While this is a simplification, it is seen from the numerical results that the phases are well-predicted and the force amplitudes are overestimated. The difference between the measured and calculated results is considered to be small given the simplification used and indicates the soundness of the proposed method. The results can be further improved by selecting appropriate frequency-dependent force coefficients for the Morison equation.

4. Conclusion

A novel approach to evaluating hydrodynamic loads on a cylinder using a combination of strip theory and Morison equation using undisturbed nonlinear wave kinematics from a nonlinear NWT is presented. This extends the application of nonlinear wave

tanks to simulate stochastic three-hour simulations with steep and breaking wave events and identify extreme wave events and provide a reasonable estimate of the extreme wave loads in the early stages of the design process. The method is verified through comparison of the analytical and numerical results for the wave kinematics in the case of a nonlinear regular wave defined by fifth-order Stokes wave theory.

The method is used to evaluate the hydrodynamic loads on a cylinder due to regular, irregular and focused waves. The calculated free surface elevation and the hydrodynamic loads are seen to be in good agreement with the measurements and imply that the wave kinematics are well represented. The utility of the model to estimate the loads on a cylinder under irregular waves with breaking wave events is demonstrated. The results show good agreement with the measurements, with some overestimation of the loads. Some nonphysical peaks are seen in the load signal which arise from the numerical treatment of wave breaking and a low-pass filter is used to resolve this. The overestimation of the hydrodynamic loads results from the use of a constant, frequency independent force coefficient. This is demonstrated by the results calculated for the higher-order wave forces using a band filter. In spite of this simplified treatment, the estimated wave forces, including forces due to breaking waves in an irregular sea state are seen to be reasonably accurate. Higher-order wave–structure interaction resulting in secondary peaks in the loading is not represented using the demonstrated approach using the undisturbed wave kinematics. The method however is useful in identifying the occurrence of such events, which can then be analysed using CFD simulations. Further studies can be conducted to identify the best practise with regard to the use of the Morison equation with NWT simulations and the determination of the frequency-dependent force coefficients.

CRediT authorship contribution statement

Csaba Pákozdi: Conceptualization, Methodology, Validation, Software, Writing – original draft. **Arun Kamath:** Writing – original draft, Revision, Visualization. **Weizhi Wang:** Writing – original draft, Visualization. **Hans Bihs:** Supervision, Software.

Declaration of competing interest

The authors declare that they have no known competing financial interests or personal relationships that could have appeared to influence the work reported in this paper.

Acknowledgements

This work is part of the “Wave Loads and Soil Support for Extra Large Monopiles" and “High Resolution Numerical Modelling of Flexible Fish Cage Structures” projects and the authors gratefully acknowledge the support from the Norwegian Research Council (grant no. 268182 and 267981).

References

[1] Frandsen S, Tarp-Johansen NJ, Hansen EA, Høgedal M, Ibsen LB, Jensen L. Offshore wind turbine design: addressing uncertainty drivers. In: 2006 European wind energy conference and exhibition. European Wind Energy Association (EWEA); 2006.
[2] Bachynski EE, Kristiansen T, Thys M. Experimental and numerical investigations of monopile ringing in irregular finite-depth water waves. Appl Ocean Res 2017;68:154–70.
[3] Kristiansen T, Faltinsen OM. Higher harmonic wave loads on a vertical cylinder in finite water depth. J Fluid Mech 2017;833:773–805.
[4] Sharma JN, Dean RG. Second-order directional seas and associated wave forces, vol. 21. 1981, p. 129–40. http://dx.doi.org/10.2118/8584-pa.
[5] Camp T, Morris M, Van Rooij R, Van Der Tempel J, Zaaijer M, Henderson A, et al. Design methods for offshore wind turbines at exposed sites. final report of the owtes project. Technical report, Garrad Hassan and Partners Ltd; 2003.
[6] IEC 61400-3. Wind turbines—part 3: Design requirements for offshore wind turbines. International Electrotechnical Commission; 2009.
[7] Grue J, Jensen A. Orbital velocity and breaking in steep random gravity waves. J Geophys Res Oceans 2012;117(C7).
[8] Grue J, Kolaas J, Jensen A. Velocity fields in breaking-limited waves on finite depth. Eur J Mech B Fluids 2014;47:97–107.
[9] Fenton D. A fifth-order Stokes theory for steady waves. J Wtrway Port Coast Oc Eng 1985;216–34.
[10] Aggarwal A, Alagan Chella M, Bihs H, Myrhaug D. Properties of breaking irregular waves over slopes. Ocean Eng 2020;216:108098.
[11] Houtani H, Waseda T, Fujimoto W, Kiyomatsu K, Tanizawa K. Generation of a spatially periodic directional wave field in a rectangular wave basin based on higher-order spectral simulation. Ocean Eng 2018;169:428–41.
[12] Li Z, Bouscasse B, Ducrozet G, Gentaz L, Le Touzé D, Ferrant P. Spectral wave explicit navier-stokes equations for wave-structure interactions using two-phase computational fluid dynamics solvers. Ocean Eng 2021;221:108513.
[13] Lawrence C, Gramstad O, Trulsen K. Variational Boussinesq model for kinematics calculation of surface gravity waves over bathymetry. Wave Motion 2021;100:102665.
[14] Jacobsen NG, Fuhrman DR, Fredsøe J. A wave generation toolbox for the open-source CFD library: Openfoam. Internat J Numer Methods Fluids 2012;70(9):1073–88.
[15] Kamath A, Alagan Chella M, Bihs H, Arntsen ØA. CFD simulations of wave propagation and shoaling over a submerged bar. Aquat Procedia 2015;4:308–16.
[16] Liu S, Ong MC, Obhrai C, Gatin I, Vukčević V. Influences of free surface jump conditions and different k- ω SST turbulence models on breaking wave modelling. Ocean Eng 2020;217:107746.
[17] Wheeler J. Method for calculating forces produced by irregular waves. J Pet Technol 1970;22(03):359–67.
[18] Bea RG, Lai NW. Hydrodynamic loadings on offshore platforms. In: Publication of: Offshore technology conference. (OTC 3064 Vol 1 Proceeding). 1978.
[19] Gravesen H, Sørensen S, Bingham T-J, Pedersen J, Vølund P, et al. Consequences of steep waves and large wave forces to offshore wind turbine design. In: 2003 European wind energy conference and exhibition. European Wind Energy Association (EWEA); 2003.
[20] Malenica S, Molin B. Third-harmonic wave diffraction by a vertical cylinder. J Fluid Mech 1995;302:203–29.
[21] Faltinsen OM, Newman JN, Vinje T. Nonlinear wave loads on a slender vertical cylinder. J Fluid Mech 1995;289:179–98.

[22] Scolan Y-M, Boulluec M, Chen X, Deleuil G, Ferrant P, Malenica S, et al. Some results from numerical and experimental investigations on the high frequency responses of offshore structures. In: 8th International conference on the behaviour of offshore structures. (CONF-9707163). 1997.
[23] Papoutsellis CE, Yates ML, Simon B, Benoit M. Modelling of depth-induced wave breaking in a fully nonlinear free-surface potential flow model. Coast Eng 2019;154:103579.
[24] Baquet A, Kim J, Huang Z. Numerical modeling using cfd and potential wave theory for three-hour nonlinear irregular wave simulations. In: ASME 2017 36th OMAE. (OMAE2017-61090). Trondheim, Norway; 2017.
[25] Grilli ST, Vogelmann S, Watts P. Development of a 3D numerical wave tank for modeling tsunami generation by underwater landslides. Eng Anal Bound Elem 2002;26(4):301–13.
[26] Ryu S, Kim M, Lynett PJ. Fully nonlinear wave-current interactions and kinematics by a BEM-based numerical wave tank. Comput Mech 2003;32(4–6):336–46.
[27] Engsig-Karup AP, Bingham HB, Lindberg O. An efficient flexible-order model for 3D nonlinear water waves. J Comput Phys 2009;228(6):2100–18.
[28] Donea J, Huerta A, Ponthot J-P, Rodriguez-Ferran A. Chapter 14. Arbitrary Lagrangian-Eulerian methods. In: The encyclopedia of computational mechanics, vol. 1. Wiley; 2004, p. 413–37. http://dx.doi.org/10.1002/0470091355.ecm009.
[29] Takashi N, Hughes TJ. An arbitrary Lagrangian-Eulerian finite element method for interaction of fluid and a rigid body. Comput Methods Appl Mech Engrg 1992;95(1):115–38.
[30] Bihs H, Kamath A, Alagan Chella M, Aggarwal A, Arntsen ØA. A new level set numerical wave tank with improved density interpolation for complex wave hydrodynamics. Comput & Fluids 2016;140:191–208.
[31] Wang W, Kamath A, Pákozdi C, Bihs H. Investigation of focusing wave properties in a numerical wave tank with a fully nonlinear potential flow model. J Mar Sci Eng 2019;7(10):375.
[32] Wang W, Kamath A, Martin T, Pákozdi C, Bihs H. A comparison of different wave modelling techniques in an open-source hydrodynamic framework. J Mar Sci Eng 2020;8(7). http://dx.doi.org/10.3390/jmse8070526.
[33] Bihs H, Wang W, Pákozdi C, Kamath A. REEF3D:: FNPF—A flexible fully nonlinear potential flow solver. J Offshore Mech Arct Eng 2020;142(4).
[34] Falgout RD, Jones JE, Yang UM. Conceptual interfaces in hypre. Future Gener Comput Syst 2006;22(1–2):239–51. http://dx.doi.org/10.1016/j.future.2003.09.006.
[35] Guang-Shan J, Chi-Wang S. Efficient implementation of weighted ENO schemes. J Comput Phys 1996;126(1):202–28.
[36] Chi-Wang S, Stanley O. Efficient implementation of essentially non-oscillatory shock-capturing schemes. J Comput Phys 1988;77(2):439–71.
[37] Wang W. Large-scale phase-resolved wave modelling for the Norwegian Coast [Ph.D. thesis], Trondheim, Norway: NTNU Norwegian University of Science and Technology; 2020.
[38] Miquel AM, Kamath A, Alagan Chella M, Archetti R, Bihs H. Analysis of different methods for wave generation and absorption in a CFD-based numerical wave tank. J Mar Sci Eng 2018;6(2). http://dx.doi.org/10.3390/jmse6020073.
[39] Wang W, Pákozdi C, Kamath A, Bihs H. A fully nonlinear potential flow wave modelling procedure for simulations of offshore sea states with various wave breaking scenarios. Appl Ocean Res 2021;117:102898.
[40] Morison JR, Johnson JW, Schaaf SA. The force exerted by surface waves on piles, vol. 2. 1950, p. 149–54. http://dx.doi.org/10.2118/950149-g.
[41] WAS-XL. WAS-XL home page. 2017, URL https://www.sintef.no/projectweb/was-xl/.
[42] Thys M. Model test report: Wave kinematics and loads. Technical Report OC2019 F-079, SINTEF Ocean; 2019.
[43] Dadmarzi FH, Thys M, Bachynski EE. Validation of hydrodynamic loads on a large-diameter monopile in regular waves. In: ASME 2019 38th international conference on ocean, offshore and arctic engineering. American Society of Mechanical Engineers Digital Collection; 2019.
[44] Zang J, Taylor PH, Morgan G, Stringer R, Orszaghova J, Grice J, et al. Steep wave and breaking wave impact on offshore wind turbine foundations–ringing re-visited. In: Proceedings of the 25th international workshop on water waves and floating bodies, Harbin, China. 2010, p. 9–12.
[45] Pákozdi C, Wang W, Kamath A, Bihs H. Definition of the vertical spacing of a sigma grid based on the constant truncation error. In: Skallerud B, Andersson HI, editors. 10. National conference on computational mechanics. 2019.
[46] Bihs H, Alagan Chella M, Kamath A, Arntsen ØA. Numerical investigation of focused waves and their interaction with a vertical cylinder using REEF3D. J Offshore Mech Arct Eng 2017;139(4). http://dx.doi.org/10.1115/1.4036206.
[47] Fornberg B. Generation of finite difference formulas on arbitrarily spaced grids, 51. 1988, p. 699. http://dx.doi.org/10.1090/s0025-5718-1988-0935077-0.
[48] Hanselman DC, Littlefield BL. Mastering MATLAB. 1st ed.. USA: Prentice Hall Press; 2011.
[49] MacCamy R, Fuchs RA. Wave forces on piles: A diffraction theory. (69). US Beach Erosion Board; 1954.
[50] DNVGL-ST-0437. Loads and site conditions for wind turbines. Standard DNV-GL, 2016.
[51] Buldakov E, Higuera P, Stagonas D. Numerical models for evolution of extreme wave groups. Appl Ocean Res 2019;89:128–40.
[52] Pákozdi C, Fouques S, Thys M, Kamth A, Wang W, Dadmarzi FH, et al. Validation of numerical wave tank simulations using reef 3d with jonswap spectra in intermediate water depth. In: Proceedings of the ASME 2020 39th international conference on ocean, offshore and arctic engineering. (OMAE2020-18298). 2020.
[53] Forristall GZ. Wave crest distributions: Observations and second-order theory. J Phys Oceanogr 2000;30(8):1931–43.
[54] Huang Z, Guo Q. Semi-empirical crest distributions of long-crest nonlinear waves of three-hour duration. In: International conference on offshore mechanics and arctic engineering, vol. 57632. American Society of Mechanical Engineers; 2017, V001T01A038.
[55] Ma Y, Tai B, Dong G, Perlin M. Experimental study of plunging solitary waves impacting a vertical slender cylinder. Ocean Eng 2020;202:107191.
[56] Esandi JM, Buldakov E, Simons R, Stagonas D. An experimental study on wave forces on a vertical cylinder due to spilling breaking and near-breaking wave groups. Coast Eng 2020;162:103778.